

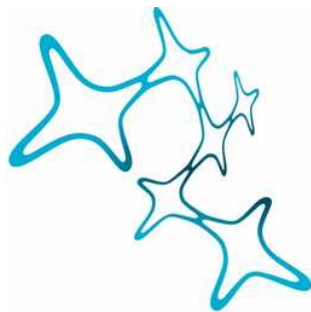
---

ANALYSIS OF *IN VIVO* GRID CELL  
ACTIVITY:

BURST FIRING AND SPATIO-  
TEMPORAL ANTICIPATION

---

Dóra Éva Csordás



Graduate School of  
Systemic Neurosciences

LMU Munich



Dissertation der  
Graduate School of Systemic Neurosciences der  
Ludwig-Maximilians-Universität München

July, 2020

Supervisor  
Prof. Dr. Andreas Herz  
Computational Neuroscience  
Ludwig-Maximilians-Universität München

First Reviewer: Prof. Dr. Andreas Herz, Prof. Dr. Anton Sirota  
Second Reviewer: Prof. Dr. Christian Leibold  
External Reviewer Prof. Dr. Richard Kempter (Berlin)

Date of Submission: 7<sup>th</sup> of July, 2020  
Date of Defense: 27<sup>th</sup> of October, 2020

# Contents

<b>1</b>	<b>Abstract</b>	<b>3</b>
<b>2</b>	<b>Introduction</b>	<b>5</b>
2.1	The Tasks of Navigation . . . . .	5
2.2	Spatially Modulated Neurons in the Hippocampal Formation . . . . .	6
2.3	Experimental Designs to Study the Neural Basis of Spatial Navigation . . . . .	8
2.4	The Contribution of Grid Cells to Navigation . . . . .	10
2.5	Temporal Activity of Grid Cells . . . . .	11
<b>3</b>	<b>First Manuscript</b>	<b>13</b>
<b>4</b>	<b>Second Manuscript</b>	<b>27</b>
<b>5</b>	<b>Discussion</b>	<b>58</b>
<b>6</b>	<b>Miscellaneous</b>	<b>67</b>
6.1	Acknowledgements . . . . .	67
6.2	Curriculum Vitae . . . . .	69
6.3	List of Publications . . . . .	72
6.4	Declaration of Author Contributions . . . . .	73



# 1 Abstract

The manner in which the brain encodes the position and movement of an animal as it navigates its environment has been a topic of intense study for decades. Interestingly, specific cell types have been identified that are thought to contribute to distinct aspects of spatial navigation. An important class, the so-called grid cells of the medial entorhinal cortex (MEC), fire spikes preferentially when the animal is near specific locations in its environment. For each grid cell, these locations form the vertices of a hexagonal lattice spanning the explored environment, which promoted the idea that the brain uses grid cells to measure the amount of distance travelled. On the other hand, many details about how the temporal firing behaviour of grid cells informs the brain about the animal's position and trajectory remain unclear. My thesis is based on two projects that address such issues of temporal coding in grid cells.

In the first study we investigated grid cells based on spike-time autocorrelations and the existence of depolarizing afterpotentials (DAPs) following single spikes. Analyzing whole-cell data from mice running on virtual tracks, we found three different groups, "sparsely bursting cells", "bursty cells with depolarizing afterpotentials" and "bursty cells without depolarizing afterpotentials". Bursty cells with prominent DAPs were mostly stellate cells in Layer II of the MEC; their interspike intervals (ISIs) reflected DAP time-scales (5-10 ms). In contrast, neither the sparsely bursting pyramidal cells in Layer III, nor the high-frequency bursters in Layer II, showed a DAP. The bursty without DAP cells had the earliest peaks in the ISI distributions, consistently around 4 ms. We hypothesized that these differences in the temporal characteristics could resemble differences on spatial coding. However, extracellular recordings from mice exploring real 2D arenas did not show strong differences in the tuning properties of the three cell groups. We next extended our analysis to non-grid principal cells in the MEC and found similar discharge characteristics. These findings suggest that depolarizing afterpotentials shape the temporal response characteristics of principal neurons in MEC with little effect on spatial properties.

In the second study we asked whether grid cells encode the animal's current location or show some predictive behavior concerning the animal's future movement. We found that the grid cell firing rate is higher when the animal moves into a firing field of that neuron ("inbound" parts of the animal's trajectory) than when it travels in an outbound direction. We could eliminate this difference by shifting spikes ahead in time or in space along the momentary movement-direction or the head-direction vector or by a given distance along the trajectory. Optimal shifts ahead were around 170 ms and 2-3 cm, respectively. With these optimal forward shifts, we have shown that grid-cell activity indeed anticipates future movements.

In short, in my thesis I have shown that DAPs influence burst firing characteristics of principal cells in the MEC and that grid cells exhibit anticipatory firing. Both findings add new aspects to the rich literature on the neural basis of spatial navigation.



## 2 Introduction

In this introduction I briefly consider the necessary prerequisites, which help to put the results of my thesis in the right context. I provide a general framework for the specific introductions of the two manuscripts in the thesis. I will give a brief introduction to spatial navigation and spatially modulated cells, especially grid cells in the brain.

### 2.1 The Tasks of Navigation

Spatial navigation is a fundamental, but complex task for the nervous system of every motile animal. It is essential to change location to obtain food, escape predators and find mates. Through an analogous example we can formulate theories of what functional subunits of neural networks could exist in the brain to solve a navigational problem.

Let us consider a hypothetical and complex example of going to the grocery store during a pandemic. One takes into account all the necessary steps and carries out all the subtasks of navigation.

The tasks of navigation - To get from A to B one needs to know:

1, Where is A? Where am I in my world/frame/city?

*I am at home.*

2, Where is B in my world/frame/city?

*The grocery store is at Bernstein street, 5.*

3, What is my unit of distance, cm/m/km?

*As I should not travel long distances, my unit of distance is meter.*

4, What is my distance and orientation relative to B?

*The grocery store is 100 m away, north from home.*

5, How to navigate safely?

*Plan a likely curved trajectory, avoiding obstacles and maintaining social distancing on the pavement.*

6, How long does it take to get to B?

*Choose the planned trajectory that is the fastest. It is crucial to spend the least time outside. Thus, one has to take the path that can be executed in the quickest way, providing the smallest probability (i.e. the shortest time window) of getting infected.*

With this example we considered the most important tasks of navigation without giving a complete overview of all the tasks. Examples for some more complicated tasks of navigation could be three-dimensional navigation, long-distance navigation along the surface of the planet or navigation in different materials, like water or air.

The brain is able to solve such a navigational problem with the help of spatially modulated cells. The functionally different cell types form a network of millions of cells which is able to compute how to navigate. In the following section we will look at how particular cells in the brain encode the sufficient parameters to carry out a navigational task.

## 2.2 Spatially Modulated Neurons in the Hippocampal Formation

In the hippocampal formation there are various types of cells responsible for computing the previously mentioned tasks to navigate successfully. The hippocampal formation is located in the medial temporal lobe of the brain and can be divided into four major regions, the hippocampus, the dentate gyrus, the subiculum and the entorhinal cortex (Figure 1.). Spatially modulated cells can be found all over the hippocampal formation.

Place cells in the hippocampus are active at a certain location in the frame (here: the city) we are in (O’Keefe & Dostrovsky, 1971). In our example, there is at least one place cell that is active when at home and another one that is active when in the grocery store. Home is also described by border cells found in the subiculum which are active when one is at the edge of a space, like the door or the walls of the house one lives in (Lever *et al.* , 2009). The spatial units of the space we are located in are represented by grid cells in the medial entorhinal cortex (Hafting *et al.* , 2005), the focus of this thesis. Like place cells, grid cell activity is spatially tuned, but unlike place cells, grid cells are active at multiple locations within the environment and these locations are arranged on the vertices of a hexagonal lattice. The hexagonal pattern can be described by the spacing between the vertices, the offset relative to the boundary and the orientation of the lattice. The orientation and distance to the grocery store are computed in concert by head direction cells in the postsubiculum and in the thalamus (Taube *et al.* , 1990), and goal-direction and goal-distance cells in the CA1 region of hippocampus (Sarel *et al.* , 2017). Head direction cells are active at a certain orientation of the head relative to external land marks. Goal-direction and goal-distance cells signal the relative orientation and the path distance to the target. Correspondingly, the activity patterns of these diverse cell types will be highly dynamic as we execute our journey to the grocery store.

Since most of the time we cannot take a straight trajectory to the store, we need to make a plan. When planning the trajectory, place cells can actually help us replay in our mind the previously known sequence of visited clues, such as corners and trees on our way to the target. The corresponding place cells fire in the same order as the remembered sites visited (Wilson & McNaughton, 1994). Hippocampal replay can both be a forward or reversed reactivation of place



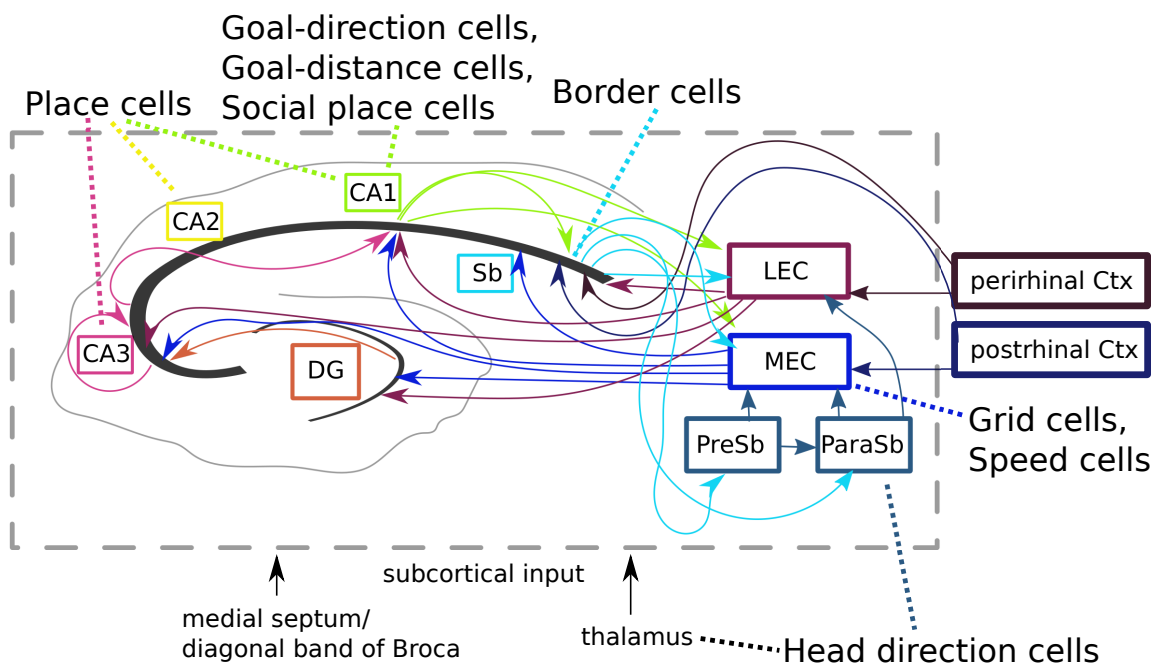


Figure 1: Schematic overview of the anatomy and the location of different spatially modulated cells in the hippocampal formation (gray dashed line). The hippocampal formation receives subcortical inputs (from the medial septum/diagonal band of Broca and thalamus) and cortical inputs (from the perirhinal and postrhinal cortex). Head direction cells are found both in the thalamus and in the dorsal portion of the presubiculum (PreSb), called postsubiculum. The lateral and the medial entorhinal cortex (LEC, MEC, respectively) receive input primarily from the pre- and parasubiculum. Grid cells are located in the MEC. The downstream area of the entorhinal cortex is the dentate gyrus (DG) and the CA3 and CA1 areas of the hippocampus. There are place cells in all three major areas of the hippocampus (CA1, CA2, CA3) and furthermore, goal-direction and goal-distance cells are also placed in the CA1 area. The primary output of the hippocampal circuit is the subiculum (Sb), where border cells can be found. This closes the circuit and synapses on the PreSb, the ParaSb, the LEC and the MEC.

cell sequences during immobility and sleep (Wilson & McNaughton, 1994; Foster & Wilson, 2006). Furthermore, another way to make a plan is preplaying a future trajectory to the goal by sequentially activating the corresponding place cells. In rodents preplay of hippocampal place cells is reported to happen when viewing the delivery of food to an unvisited part of an environment (Olafsdottir *et al.*, 2015).

Importantly, to avoid accidents, we have to plan ahead where we will be just moments ahead given the speed at which we are moving. The various cells of the hippocampal formation can calculate our future position to provide this information. Head direction cells for example, anticipate future head directions by up to 95 ms (Stackman Jr & Taube, 1998). In turn, place and grid cells

anticipate future spatial locations by 30-120 ms (Muller & Kubie, 1990), (Sharp, 1999) and 50-80 ms (Kropff *et al.* , 2015), respectively. Furthermore, to adapt to modifications in the known environments (like the appearance of a puddle on the pavement), place cells change the locations or the intensities at which they prefer to be active (Cressant *et al.* , 2002). Also, so-called social place cells in the CA1 hippocampal area signal the position of others in the environment (Omer *et al.* , 2018). Here, they can fire if there is a person passing by very closely, practically alerting us so we can re-plan the trajectory to avoid infection. When going to the store, we cannot completely avoid human contact, but we can reduce the probability of being exposed to infectious subjects, by navigating faster on the street, thus having ensuring a smaller time window spent around others. For this, speed information can be read out from speed cells in the medial entorhinal cortex, which increase their firing rate as the animal moves faster (Kropff *et al.* , 2015).

It is obvious that no single cell type described can encode our entire trajectory to the store. Only the tightly coordinated activity of the brain’s spatially modulated cells can accomplish such a computationally challenging task. Although our example is of humans, the specific cells introduced here are mainly studied in rodents. Figure 1 shows their anatomical location in the hippocampal formation.

### 2.3 Experimental Designs to Study the Neural Basis of Spatial Navigation

To identify and study the navigational functionality of the cells mentioned above one needs to have access to their electrical activity. This is traditionally performed by implanting electrodes, often in the form of four bundled wires, called tetrodes, in the brain of rodents, usually in rats or mice. The tetrode records the so-called local field potential in the vicinity of the electrodes, an electric signal representing the superposition of various different neural dynamics going on in parallel, such as action potentials and synaptic activity (Buzsáki *et al.* , 2012). The further away the signal’s source is from the tetrode, the smaller the recorded amplitude and the broader the signal’s wave form. However, when the tetrode happens to be particularly close to the cell bodies of individual neurons, it can furthermore detect the spike activity of those neurons. Using the differences between the four signals recorded simultaneously with the tetrode, one can extract and separate the spike activity of individual neurons within the group (so-called single units) and assign unique spike-times to the respective cells (Figure 2A).

While such recordings are ideal for freely moving animals, they provide little insight into the processes underlying the cells’ firing behavior. To overcome this limitation, whole-cell recordings serve as a complementary method to understand how and why neurons may fire in specific temporal patterns. Here, the intracellular membrane-potential dynamics are of particular importance and is usually measured with patch-clamp electrodes targeted to individual neurons. It should be noted

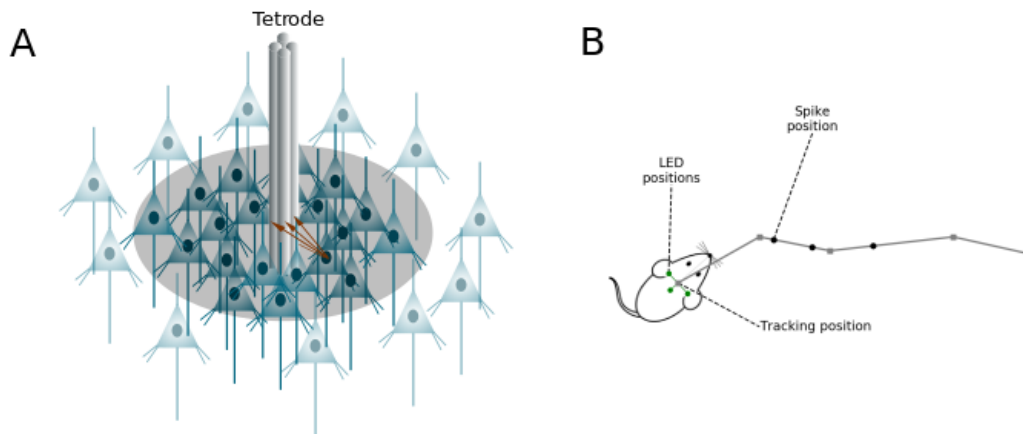


Figure 2: Experimental design to study navigation in the rodent brain. **A**, Recording of the local field potential and different cells' activities. The four electrodes of the tetrode record the activity of the close-by cells (in the example shown: pyramidal neurons in the gray area). The action potentials of one cell are recorded with different amplitudes on the 4 electrodes because all the 4 electrodes have a different distance from the cell (arrows). The signal-to-noise ratio of cellular activities decays with increasing distance. **B**, Recording of the animal's trajectory and its position when spikes are generated. In this example, there were three LEDs (green dots) placed on the head of the animal, from which at every sampling time the tracking position (gray squares) was recorded by a camera placed above the experimental arena (not shown). The positions of a cell's spikes (black dots) can then be calculated from the recorded spike-times from the tetrodes (A) by interpolation along the recorded trajectory.

that although these methods are also possible *in vivo*, they require head-fixed recordings in virtual-reality settings, thus restricting the natural movement behavior of the animals (see, for example, Domnisoru *et al.* (2013)).

For experiments with which the neural data of spatially modulated neurons are collected *in vivo*, the animal is usually put into a box or a circular arena. The animal is expected to move around freely and cover the environment with its movements. To encourage this behavior, the experimenters typically throw in chocolate chips to random spots in the arena. A camera above the arena records the location of the animal using tracking LEDs on its head. In the end, one acquires two datasets recorded in parallel, one containing the spike-times of one or multiple neurons and the other one the position of the animal over time. From the spike-times one can then compute the specific position of the animal that corresponded to a particular spike (i.e., where the animal was when a spike of a cell was fired) (Figure 2B).

## 2.4 The Contribution of Grid Cells to Navigation

In this thesis, the neural basis of navigation is studied by analyzing the activity of grid cells. Grid cells are located in the medial entorhinal cortex, an input area to the hippocampus, where place cells are located. When the animal explores its environment grid cells appear to activate in a regular manner. They fire action potentials at multiple locations, which together form a hexagonal lattice (Figure 3) (Fyhn *et al.* , 2004; Hafting *et al.* , 2005). A region where spikes accumulate is called a grid field; its member spikes are denoted by red circles in Figure 3, the center of the grid field by a black asterisk. Grid-cell like representations were shown for rodents, bats and humans, in two-dimensional, three-dimensional, close to natural and virtual navigational tasks as well (Fyhn *et al.* , 2004; Doeller *et al.* , 2010; Yartsev *et al.* , 2011; Hayman *et al.* , 2011).

The regular firing patterns of grid cells could emerge from a path integration-dependent attractor network of cells providing a metric representation of the spatial environment (Hafting *et al.* , 2005). In agreement with this theory some grid cells were also experimentally shown to conjunctively represent position, direction and velocity (Sargolini *et al.* , 2006). Remarkably, when changing recording environments the positional relationship between grid cells is maintained, suggesting, unlike place cells their activity is independent of the contextual details of individual environments (Fyhn *et al.* , 2007). Such a rigid structure of the grid map combined with its spatial periodicity could serve as a stable component of the brains metric for a local space during navigation (Moser *et al.* , 2008; Fyhn *et al.* , 2007). Note, however, that the activity level within a grid field does depend on contextual cues (Diehl *et al.* , 2017).

The entire population of grid cells can be divided into different grid modules (Stensola *et al.* , 2012). In each module, grid cells have similar spacing (grid scales) and orientation between the grid fields, whereas their offset, i.e., the relative position of fields to the boundaries varies. Also, the modules are topographically arranged along the dorsoventral axis of the MEC, small inter-field distances predominate the dorsal part and high inter-field distances predominate the ventral part. The grid scales of the 4-10 different modules follow a geometric progression rule with a scale factor approximately around 1.42 (Stensola *et al.* , 2012). Theoretical work of Mathis *et al.* (2012) showed with that such a nested, modular organization the grid code can exceed the best possible place code with the same number of neurons.

I chose to study the neural basis of navigation in grid cells because they seem to be a stable spatially modulated subset of cells providing a rather rigid input to the more sensitive set of place cells.

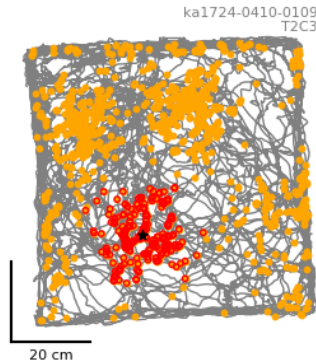


Figure 3: The recording of one grid cell in a 70\*70 cm arena while a mouse was foraging for 20 minutes. Grey line: the trajectory of the animal. Yellow dots show the position of the animal when an action potential was fired by the recorded grid cell. Red circles denote the positions of action potentials belonging to one particular grid field, detected by automatic clustering of the spike positions. The black asterisk denotes the center of the grid field. The name of the animal, the tetrode number (TX) and the cell number (CY) is indicated by the gray text. Data recorded by Latuske *et al.* (2015).

## 2.5 Temporal Activity of Grid Cells

Grid cells are interesting not only because of their remarkable spatial firing properties, but also because they exhibit non-trivial activity in the temporal domain. One widely studied temporal property of spatially tuned cells is the so-called theta-phase precession. Compared to the ongoing, large-scale theta oscillation (7-12 Hz) in the hippocampus and medial entorhinal cortex, cells fire at earlier and earlier phases of these cycles as the animal is moving through a firing field. This was shown not only for place cells (O’Keefe & Recce, 1993), but also for grid cells (Hafting *et al.* , 2008; Reifenstein *et al.* , 2012).

Given the temporal order in which the fields are visited, from differently phase precessing place or grid cells the so-called theta sequences can arise, first reported by Foster & Wilson (2007). Theta sequences are the temporal sequences of spikes of different place or grid cells in one theta cycle. During navigation spikes of cells’ whose fields are ahead of the animal will appear at the late phases of the cycle, whereas spikes of cells corresponding to fields of ”now” and the ”past” would be at earlier and earlier phases of that same theta cycle. For grid cells, the firing rate at the ”look ahead” phases of theta cycle was higher than at the ”reset” phases (Kropff *et al.* , 2015).

There is a debate in the literature about whether theta cycles contribute to the formation of the grid pattern. Brandon *et al.* (2011) reported that in rodents with inactivation of the medial septum, the strength of theta activity in the medial entorhinal cortex was reduced and grid cells lost their spatial periodicity. However, in the entorhinal cortex of bats grid cells existed in the

absence of continuous theta band oscillations, although approximately second long "theta-bouts" were reported during crawling (Yartsev *et al.* , 2011).

Nested within the slower theta rhythm are network oscillations with frequency in the high gamma range (60-120 Hz) (Chrobak & Buzsáki, 1998; Colgin *et al.* , 2009). In the MEC, gamma oscillations have clock-like features suitable as reference signals for multiplexing temporal codes within rate-coded grid firing fields (Pastoll *et al.* , 2013). Furthermore, the cells exhibit burst behavior, i.e., they fire packages of spikes with interspike intervals in the 5-20 ms range. But not all cells burst in the same manner. Some fire frequently in bursts while others show little bursting if at all (Latuske *et al.* , 2015). This bursting behavior could be observed because of the dense expression of perineural nets around reelin-expressing stellate cells in the Layer-II of MEC, which was shown to support plasticity and bursting behavior (Lensjo *et al.* , 2017a,b). Also, early peaks in the pairwise spike-time cross-correlations of grid cells reflected the corresponding spatial tuning offsets, not only during exploration but also in REM and non-REM states (Trettel *et al.* , 2019; Gardner *et al.* , 2019). The few milliseconds delay between the firing of cell pairs supports the theory that grid cells are recurrently connected (Fuhs & Touretzky, 2006; McNaughton *et al.* , 2006; Burak & Fiete, 2009; Navratilova *et al.* , 2012). As there are many open questions regarding grid cell firing patterns in the temporal domain, we focused on two questions regarding the temporal firing behavior of grid cells.

First, we studied the burst behavior of grid cells. We investigated whether the so-called depolarizing afterpotential (DAP) following a single spike might underlie burst behavior *in vivo*. DAPs are "bump-like", 5-10 ms long deflections in the membrane-potential dynamics following an action potential and a short fast after-hyperpolarization. This *in vivo* analysis was strongly motivated by *in vitro* results reported by Alessi *et al.* (2016), who had found that there can be a second spike sitting on the DAP if the cell was well hyperpolarized before triggering the spike. Furthermore, this was shown to be true for stellate cells, but not for pyramidal cells (Alessi *et al.* , 2016). We also studied whether the existence of depolarizing afterpotentials carries navigational information or encodes a specific position relative to the hexagonal firing pattern.

Second, we asked whether grid cells could plan ahead in time and signal a future position of the animal on its current trajectory. When navigating (i.e. in our example trip to the grocery store), one must always plan a little forward along the path, for example: look ahead on the pavement when walking. It also seems like a plausible scenario for grid cells that they rather signal a future position along the trajectory (de Almeida *et al.* , 2012; Kropff *et al.* , 2015), so one can plan and avoid close encounters and accidents. We explored whether this anticipation was spatial or temporal.

### 3 First Manuscript

# Spike Afterpotentials Shape the *In Vivo* Burst Activity of Principal Cells in Medial Entorhinal Cortex

Dóra É. Csordás, Caroline Fischer, Johannes Nagele,  Martin Stemmler, and  Andreas V.M. Herz

Bernstein Center for Computational Neuroscience Munich and Faculty of Biology, Ludwig-Maximilians-Universität München, Martinsried-Planegg 82152, Germany

Principal neurons in rodent medial entorhinal cortex (MEC) generate high-frequency bursts during natural behavior. While *in vitro* studies point to potential mechanisms that could support such burst sequences, it remains unclear whether these mechanisms are effective under *in vivo* conditions. In this study, we focused on the membrane-potential dynamics immediately following action potentials (APs), as measured in whole-cell recordings from male mice running in virtual corridors (Domnisoru et al., 2013). These afterpotentials consisted either of a hyperpolarization, an extended ramp-like shoulder, or a depolarization reminiscent of depolarizing afterpotentials (DAPs) recorded *in vitro* in MEC principal neurons. Next, we correlated the afterpotentials with the cells' propensity to fire bursts. All DAP cells with known location resided in Layer II, generated bursts, and their interspike intervals (ISIs) were typically between 5 and 15 ms. The ISI distributions of Layer-II cells without DAPs peaked sharply at around 4 ms and varied only minimally across that group. This dichotomy in burst behavior is explained by cell-group-specific DAP dynamics. The same two groups of bursting neurons also emerged when we clustered extracellular spike-train autocorrelations measured in real 2D arenas (Latuske et al., 2015). Apart from slight variations in grid spacing, no difference in the spatial coding properties of the grid cells across all three groups was discernible. Layer III neurons were only sparsely bursting (SB) and had no DAPs. As various mechanisms for modulating ion-channels underlying DAPs exist, our results suggest that temporal features of MEC activity can be altered while maintaining the cells' overall spatial tuning characteristics.

**Key words:** bursts; grid cells; medial entorhinal cortex; spatial navigation; spike afterpotentials; whole-cell recording *in vivo*

## Significance Statement

Depolarizing afterpotentials (DAPs) are frequently observed in principal neurons from slice preparations of rodent medial entorhinal cortex (MEC), but their functional role *in vivo* is unknown. Analyzing whole-cell data from mice running on virtual tracks, we show that DAPs do occur during behavior. Cells with prominent DAPs are found in Layer II; their interspike intervals (ISIs) reflect DAP time-scales. In contrast, neither the rarely bursting cells in Layer III, nor the high-frequency bursters in Layer II, have a DAP. Extracellular recordings from mice exploring real 2D arenas demonstrate that grid cells within these three groups have similar spatial coding properties. We conclude that DAPs shape the temporal response characteristics of principal neurons in MEC with little effect on spatial properties.

## Introduction

Principal neurons in the superficial layers of medial entorhinal cortex (MEC) show rich temporal behavior, from slow depolarization ramps (Domnisoru et al., 2013; Schmidt-Hieber and

Häusser, 2013), spike locking and phase precession in the  $\theta$  band (Hafting et al., 2008; Reifensstein et al., 2012), to  $\gamma$ -band activity (Chrobak and Buzsáki, 1998; Colgin et al., 2009) and burst sequences with instantaneous firing rates of up to 300 Hz (Latuske et al., 2015). The spatial firing fields of one particular MEC cell class, namely grid cells, form hexagonal lattices spanning the explored 2D environment (Hafting et al., 2005). Notably, not every grid cell participates to the same degree in these temporal phenomena. In particular, there are two subclasses of grid cells, those that burst frequently and those that do not or only rarely generate bursts (Mizuseki et al., 2009; Latuske et al., 2015; Ebbesen et al., 2016). But what is the mechanism behind the MEC bursts and what role do they play for spatially selective neurons, such as grid cells?

Received Oct. 28, 2019; revised Apr. 3, 2020; accepted Apr. 11, 2020.

Author contributions: D.É.C., C.F., J.N., M.S., and A.V.M.H. designed research; D.É.C., C.F., and J.N. performed research; D.É.C., C.F., and J.N. analyzed data; D.É.C., C.F., J.N., M.S., and A.V.M.H. wrote the paper. D.É.C., C.F., and J.N. contributed equally to this work.

This work was supported by the German Federal Ministry for Education and Research Grant 01GQ0440.

The authors declare no competing financial interests.

Correspondence should be addressed to Andreas V. M. Herz at herz@bio.lmu.de.

<https://doi.org/10.1523/JNEUROSCI.2569-19.2020>

Copyright © 2020 the authors



In this study, we tested the hypothesis that burst activity of principal neurons in MEC is shaped by cell-intrinsic membrane-potential dynamics. While extrinsic factors, such as  $\theta$ -band coupling in MEC Layer-II stellate cells change the likelihood of burst generation (Alonso and Klink, 1993; Engel et al., 2008; see also Hasselmo, 2014; Newman and Hasselmo, 2014) and the timing of spikes within a burst could reflect the arrival of strongly coincident synaptic input, we focus on the short-term dynamics that are triggered in the wake of an action potential (AP).

Indeed, slice experiments have shown that depolarizing afterpotentials (DAPs) arise in a majority of principle cells in superficial MEC layers (Alonso and Klink, 1993; Canto and Witter, 2012). DAPs are at the center of triphasic deflections following an AP, sandwiched between fast and medium after-hyperpolarization (fAHP and mAHP). The DAP maximum occurs some 5–10 ms after the AP and peaks a few millivolts above the fAHP minimum. In stellate cells, DAPs become more pronounced when neurons are hyperpolarized, whereas the reverse is true for pyramidal neurons (Alessi et al., 2016). Not all cell types associated with grid-like rate maps have DAPs *in vitro*, however. In particular, Layer-III neurons are reported to have no DAPs (Canto and Witter, 2012).

DAPs do not only agree in their relevant time scale with intraburst interspike intervals (ISIs); *in vitro*, DAPs also play a causal role for bursting. Alessi et al. (2016) reported that during DAPs the AP current threshold was reduced such that the cells' average excitability increased by over 40%. Conversely, neurons without strong DAPs did not burst at the beginning of an AP train (Canto and Witter, 2012).

To test the functional relevance of DAPs under *in vivo* conditions, we analyzed whole-cell recordings from mice moving on a virtual linear track (Domnisoru et al., 2013) and could show that DAPs play a decisive role for burst firing in MEC Layer-II neurons: Cells with DAPs were bursty and their intraburst ISIs were compatible with the DAP mechanism. ISI distributions of the other Layer-II cells were highly uniform and had a sharp peak at  $4.1 \pm 0.2$  ms (SD across this cell group). The remaining neurons were sparsely bursting (SB) and those with known location resided in Layer III, apart from one pyramidal cell in Layer II. The results are compatible with our findings for extracellular recordings from open-field arenas (Latuske et al., 2015). In addition, bursty cells with and without DAP did not differ in their spatial coding properties, apart from a slight change in grid spacing. As the ionic conductances that support DAPs are subject to modulatory factors, our analysis suggests that temporal features of grid-cell activity can be altered to serve different functions without affecting the cells' qualitative spatial tuning characteristics.

## Materials and Methods

### Data

We analyzed data from two separate studies in navigating wild-type (C57BL/6) male mice. Dataset D (Domnisoru et al., 2013) contained voltage traces from whole-cell recordings sampled at 20 kHz in head-fixed animals. These mice ran on cylindrical treadmills through virtual corridors. Dataset L (Latuske et al., 2015) contained tetrode data (sampling frequency: 20 or 24 kHz) obtained during movements in a real square arena ( $70 \times 70$  cm).

### Cell selection

#### Dataset D

The original dataset contained recordings from 51 cells of which 27 had been classified as grid cells by Domnisoru et al. (2013). One grid-cell recording was partially corrupted and excluded. Two grid cells had mean firing rates above 10 Hz and were removed to allow for an unbiased

comparison with dataset L, which contained only cells with firing rates below 10 Hz to exclude interneurons. From the 24 neurons that had been classified as non-grid cells two cells had firing rates above 10 Hz and the APs of six other cells did not meet our criteria (see below, Membrane-potential dynamics). This resulted in 40 neurons from dataset D, namely 24 grid cells and 16 non-grid cells.

#### Dataset L

After removing cells for which the animal trajectories showed artifacts, 522 principal cells were identified using the same criterium (mean firing rate  $< 10$  Hz) as in Latuske et al. (2015). Out of those cells, 115 cells had been classified as grid cells by these authors. Ten of the 522 cells were not considered further as their ISI distributions differed strongly from all other cells in that they had not a single ISI below 8 ms. Similarly, to avoid artifacts in the cluster analysis of the cells' spike-time autocorrelations, seven cells with sparse autocorrelations were removed (see below for details). Altogether, this led to 505 cells in dataset L, 112 grid cells and 393 non-grid cells.

### Spike-train characterization

The firing rate of a cell was defined as number of spikes divided by the total duration of the recording. For the graphical illustrations, spike-time autocorrelations and ISI distributions were calculated from binned data (bin width: 1 ms). To compute the peak location and width of ISI distributions, the recorded time difference between each pair of successive spikes was represented by a Gaussian kernel with a SD of 1 ms, centered at the measured time difference. These individual kernel density (KD) estimates were summed up across the entire recording. The analogous procedure was used for autocorrelations.

The location of the ISI peak was determined as the ISI for which the KD estimate was maximal. Similarly, the width of the ISI distribution was defined as full width at half maximum. The mean ISI and its SD were calculated from all ISIs, the coefficient of variation (CV) was defined as the ratio of SD to mean.

A burst was defined as a sequence of at least two spikes with ISIs shorter than 8 ms. The fraction of ISIs smaller than 8 ms was calculated relative to all ISIs and serves as a measure for the cell's burstiness. An event is a burst or an isolated spike. The fraction of single spikes was defined as the number of spikes that do not belong to a burst divided by the number of all events.

### Principal-component analysis (PCA)

For both datasets, autocorrelations were calculated for time lags between 0 ms and  $\tau_{\max} = 50$  ms. To weigh all neurons equally autocorrelations were normalized to unit area. Principal components were calculated after binning (bin width: 1 ms). To reduce spurious effects caused by sparse normalized autocorrelations, cells with  $> 75\%$  empty bins (the maximum value for dataset D) were removed (one grid cell and six non-grid cells in dataset L). For the same reason, five (two) cells of dataset D (dataset L) that had relatively few spikes ( $< 130$ ) were excluded when PC components were calculated but are included in the further analysis. To test the robustness of the PCA of the D data, the maximal time lag  $\tau_{\max}$  was varied between 30 and 100 ms (see also Results).

### Identification of neuron classes

For the D dataset, visual inspection of the 2D space spanned by the first two PCs suggested two main cell groups, whose arrangement was determined by k-means clustering with  $k = 2$  clusters. To test the robustness of the k-means clustering for the L dataset, cluster analyses were performed on the 50-dimensional binned autocorrelations as well as in PC spaces with  $N = 2-4$  dimensions. The clustering quality was estimated through silhouette scores (Rousseeuw, 1987).

### Membrane-potential dynamics

The whole-cell voltage traces contained sizeable fluctuations that reflected synaptic inputs and potential movement artefacts. To obtain reliable information about the membrane potential before and after an AP, AP-triggered averaging was performed. The APs themselves varied in amplitude and width, both within and across the different recordings,

suggesting that the recording quality varied in time; the slowly decaying AP amplitudes and increasing width of some cells indicated run-down effects. To guarantee a good recording quality and to obtain reliable estimates of the subthreshold membrane-potential dynamics on the time scales relevant for fAHPs and DAPs, we focused on well isolated APs (no further APs within 25 ms before and after the trigger AP), and required the individual AP amplitudes to be larger than 40 mV (measured relative to the membrane potential 10 ms before the AP maximum) and APs width (full width at half height) to be smaller than 1 ms.

The pre-AP voltage slope was calculated from the cell's average AP-triggered voltage trace within the last 10 ms before AP onset; AP onset was determined by a threshold crossing (15 mV/ms) in the first derivative of the average AP-triggered voltage trace. For single APs, the AP threshold was determined by the point of maximal curvature in the voltage trace (after Gaussian-filtering the voltage trace with  $\sigma = 0.1$  ms).

For the intraburst voltage traces shown in Figure 1C, we collected all first and second APs (amplitude >40 mV, width <1 ms) within a burst, i.e., all APs following an ISI longer than 8 ms and followed by an ISI shorter than 8 ms ("first APs") and all APs following a first AP with an ISI shorter than 8 ms ("second APs"), respectively. To illustrate the time evolution of the membrane potential, we either aligned the voltage traces at the first AP and cut the trace when the threshold for the second AP was reached (Fig. 1C, left panels) or aligned the traces at the second AP (Fig. 1C, right panels). In that case, the highlighted traces start at two AP-widths after the first AP and end at the threshold crossing of the third AP in the burst or 8 ms after the second AP, whichever comes first. Mean voltage traces (Fig. 1C, black lines) are calculated from these truncated samples to minimize influences by AP upstrokes or downstrokes.

For cells with DAPs, the fAHP amplitude  $\Delta V_{fAHP}$  was defined as the average voltage minimum during the fAHP relative to the voltage at AP onset. This means that  $\Delta V_{fAHP}$  is negative for DAP cells (Fig. 1). The DAP-deflection  $\Delta V_{DAP}$  was defined as the difference between the voltage level at the DAP peak and at the minimum of the preceding fAHP. It is positive for cells with DAPs. The time interval between the AP peak and the following fAHP minimum is denoted by  $\Delta t_{fAHP}$ , the time interval between the AP peak and the following DAP maximum is called  $\Delta t_{DAP}$ .

To compare the after potentials of all recorded neurons, the definitions of  $\Delta V_{fAHP}$  and  $\Delta V_{DAP}$  had to be generalized to cells without DAP. This was done (1) for grid cells only, and (2) for all neurons. To this end, we calculated the population averages  $-\Delta t_{fAHP}$  and  $-\Delta t_{DAP}$  across the respective DAP cells (grid cells:  $n = 8$ , all neurons:  $n = 15$ ). We then used these mean time intervals (grid cells:  $\Delta t_1 \equiv -\Delta t_{fAHP} = 1.8 \pm 0.4$  ms,  $\Delta t_2 \equiv -\Delta t_{DAP} = 4.6 \pm 1.2$  ms, all neurons:  $\Delta t_1 \equiv -\Delta t_{fAHP} = 2.0 \pm 0.5$  ms,  $\Delta t_2 \equiv -\Delta t_{DAP} = 5.4 \pm 2.3$  ms) to determine voltage changes corresponding to  $\Delta V_{fAHP}$  and  $\Delta V_{DAP}$  for cells without DAP. These are called  $\Delta V_1$  and  $\Delta V_2$ , respectively. For notational simplicity, we will use these terms for DAP cells, too, but here, they denote the  $\Delta V_{fAHP}$  and  $\Delta V_{DAP}$  values measured at the cell-specific  $\Delta t_{fAHP}$  and  $\Delta t_{DAP}$  values.

To characterize the subthreshold behavior following the first AP within a burst, we determined  $\Delta V_1$  and  $\Delta V_2$  values from the traces between the first and second AP and used the cell-specific  $\Delta t_1$

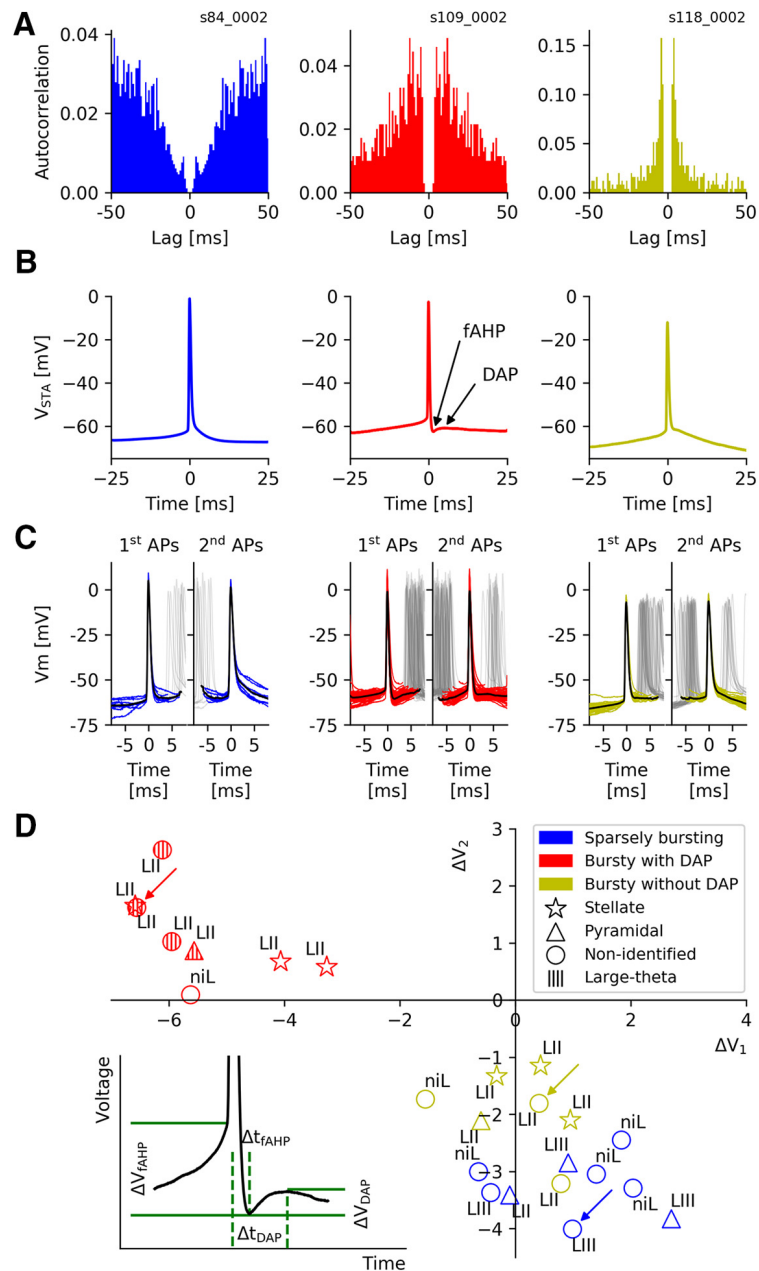


**Figure 1.** Spike afterpotentials of MEC grid cells from mice moving in virtual corridors. **A**, Typical examples of grid-cell burst behavior. Left panel, Autocorrelation function of a SB cell. Middle panel, A bursting cell with broad autocorrelation flanks. Right panel, A bursting cell with sharply peaked autocorrelation. Note the different scale on the y-axis. **B**, Grid cells differ in their spike afterpotentials, as shown by the spike-triggered averages of the voltage traces of isolated APs (no further APs within 25 ms before and after the trigger AP). Left panel, A monotone repolarization that is gradually slowing down. Middle panel, fAHP followed by a DAP. Right panel, A short repolarization that abruptly turns into a much slower voltage decay, which may include an initial flat shoulder. **C**, These dynamics occur during bursts, too, as shown by voltage traces around the first and second AP in a burst (left and right subpanels, respectively). The fAHP/DAP complex is more pronounced after the first spike (middle panel), and the membrane potential decreases more rapidly after the second spike in the two example cells without fAHP/DAP complex, in agreement with the lack (left panel) or reduction (right panel) of further spikes in the burst. **D**, Characterization of spike afterpotentials. Inset, Definition of parameters. Main panel, Group data. To characterize afterpotentials for cells without DAPs, the two parameters  $\Delta V_1$  and  $\Delta V_2$  take the role of  $\Delta V_{fAHP}$  and  $\Delta V_{DAP}$ . The new parameters are determined in the same way as  $\Delta V_{fAHP}$  and  $\Delta V_{DAP}$ , at times  $\Delta t_1$  and  $\Delta t_2$ , respectively. These times are obtained from averages of  $\Delta t_{fAHP}$  and  $\Delta t_{DAP}$  across the population of DAP cells. To simplify the notation, the terms  $\Delta V_1$  and  $\Delta V_2$  (instead of  $\Delta V_{fAHP}$  and  $\Delta V_{DAP}$ ) are used for DAP cells, too.

and  $\Delta t_2$  values calculated for isolated APs. For one DAP cell,  $\Delta t_1$  exceeded 8 ms so that this analysis could not be applied. Similarly, the second APs of six other cells did not meet the AP-width criterium so that in total, seven cells had to be excluded.

### Spatial coding properties

For dataset L, firing rate maps were computed as in Latuske et al. (2015). Based on these maps and their spatial autocorrelations, grid spacings were computed; grid scores and head-direction scores were calculated as in Sargolini et al. (2006), the spatial information as in Skaggs et al. (1996).

### Experimental design and statistical analysis

We analyzed data recorded by Domnisoru et al. (2013) and Latuske et al. (2015) and refer the reader to these two publications for details on the experimental design. All our analyses were performed in Python 2.7.6. Specific statistical tests used are stated throughout the text. The Kruskal–Wallis test, the Kolmogorov–Smirnov test, the  $\chi^2$  test, and the median tests are taken from `scipy.stats` (0.17.0, RRID: SCR\_008058). For an overview over SciPy, see Virtanen et al. (2020). The linear regression, the PCA and the k-means clustering are taken from `scikit-learn` (0.19.2, RRID: SCR\_002577; Pedregosa et al., 2011). Unless noted otherwise, all errors are reported as SDs.

### Bootstrapping

To assess the fAHP and DAP parameters, we bootstrapped the AP-triggered voltage traces of a cell by using sampling with replacement and repeated this procedure 10,000 times to obtain mean values and standard errors.

## Results

The temporal firing characteristics of principal neurons in the MEC of behaving rodents vary strongly from cell to cell, even if their mean firing rates are almost identical (Latuske et al., 2015). Some neurons rarely fire with ISIs shorter than 8 ms; their spike-time autocorrelations have a pronounced dip at short time lags (Fig. 1A, left). In other cells, the autocorrelation peaks in the 5- to 15-ms range with broad flanks (Fig. 1A, middle); yet other cells have distinct autocorrelations that are sharply peaked at even shorter lags (Fig. 1A, right). The second and third group of neurons were collectively termed “bursty” by Latuske et al. (2015), who did not distinguish between the two groups, whereas the first group has been called “non-bursty” by these authors. Since non-bursty neurons generate bursts from time to time, too, we will call them “sparsely bursting” (SB), in line with Simonnet and Brecht (2019).

We wondered whether differences in the *in vivo* spike patterns of bursty neurons could be explained at a mechanistic level by differences in their intrinsic single-cell dynamics and whether, for the spatially tuned cells within the total population, differences in the cells’ temporal discharge patterns were reflected in their spatial tuning properties. To this end, we analyzed whole-cell recordings from mice moving on a linear track in virtual reality (Domnisoru et al., 2013) and extracellular recordings from mice navigating in 2D environments (Latuske et al., 2015).

We start with an analysis of grid cells and then extend our approach to non-grid cells. Before doing so, we note that recent work shows that true grid-cell firing in a virtual environment is only seen if the animal is free to rotate its head in a virtual environment (Chen et al., 2019). For this reason, when we use the term “grid cells” for the cells recorded by (Domnisoru et al., 2013) under head fixation, such a cell should be understood as a “putative grid cell.”

### Grid cells differ in the voltage deflections following an AP

We first focus on the intracellular linear-track data as these provide information about both spike times and membrane-potential dynamics.

The time courses of the membrane potentials recorded by Domnisoru et al. (2013) show striking cell-to-cell differences within the first 10 ms following an AP. Three distinct types of behavior can be distinguished from the spike-triggered voltage traces of isolated APs (such that no other APs occurred within 25 ms before or after the trigger AP): (1) a monotone repolarization that gradually slows down (Fig. 1B, left panel); (2) a fAHP followed by a DAP (Fig. 1B, middle panel); and (3) a short repolarizing phase that abruptly turns into a much slower voltage decay, which may include a flat shoulder (Fig. 1B, right panel).

Are these characteristic features only expressed when a cell fires isolated APs or can they also be observed during episodes of high spike activity? To answer this question, we analyzed bursts (Fig. 1C), defined as AP sequences with intraburst ISIs of <8 ms. Distinguishing between the voltage traces around the versus second AP in a burst (Fig. 1C, left vs right subpanels), shows that in cells with a fAHP/DAP complex, this voltage excursion is more pronounced after the first spike (Fig. 1C, middle panel). In the two cells without fAHP/DAP complex, the membrane potential decreases more rapidly after the second spike, in agreement with the lack (Fig. 1C, left panel) or strongly reduced number (Fig. 1C, right panel) of further APs in the burst.

To quantify these distinct behaviors, we used parameters that capture two salient features of cells exhibiting DAPs, the voltage minimum during the fAHP and the voltage peak during the DAP (Fig. 1D, lower left inset). The “fAHP-depth”  $\Delta V_{\text{fAHP}}$  measures the voltage minimum relative to the membrane potential at AP onset. This minimum occurs at some time  $\Delta t_{\text{fAHP}}$  after the AP peak. The “DAP-deflection”  $\Delta V_{\text{DAP}}$  measures the difference between the membrane potential at the DAP peak and the fAHP minimum. The DAP peak is attained at some time  $\Delta t_{\text{DAP}}$  after the AP peak (Fig. 1D).

To extend the  $\Delta V_{\text{fAHP}}$  and  $\Delta V_{\text{DAP}}$  measures to voltage traces of cells with no detectable DAP, two time intervals corresponding to  $\Delta t_{\text{fAHP}}$  and  $\Delta t_{\text{DAP}}$  need to be defined. For concreteness, we used the population means across all grid cells with a DAP ( $n = 8$ ), resulting in  $\Delta t_1 \equiv -\Delta t_{\text{fAHP}} = 1.8 \pm 0.4$  ms and  $\Delta t_2 \equiv -\Delta t_{\text{DAP}} = 4.6 \pm 1.2$  ms. We then determined the voltage differences corresponding to  $\Delta V_{\text{fAHP}}$  and  $\Delta V_{\text{DAP}}$  at these two time points, and named them  $\Delta V_1$  and  $\Delta V_2$ , respectively. For DAP cells, we define  $\Delta V_1 = \Delta V_{\text{fAHP}}$  and  $\Delta V_2 = \Delta V_{\text{DAP}}$  to simplify the notation. These settings mean that cells with a shoulder or slow voltage decay (Fig. 1B, right panel) have zero or small  $\Delta V_2$  regardless of their  $\Delta V_1$  value, whereas large negative  $\Delta V_2$  values indicate a strong decline in membrane potential until around 5 ms after the AP.

Within the parameter space spanned by  $\Delta V_1$  and  $\Delta V_2$ , neurons fall into two distinct groups (Fig. 1D), cells with a pronounced DAP (negative  $\Delta V_1$  and positive  $\Delta V_2$ ) and cells with no detectable DAP (negative  $\Delta V_2$ ), which typically have also no fAHP (positive  $\Delta V_1$ ). Results from a bootstrapping analysis (see Materials and Methods) underscore the reliability of the  $\Delta V_1$  and  $\Delta V_2$  estimates (Fig. 2A). Whether we measured APs within bursts or isolated APs did not qualitatively change the scatter of data points in the  $\Delta V_1$ – $\Delta V_2$  plane nor the relation between the cell groups (Fig. 2B).

All measured neurons that had a DAP and whose location was known resided in Layer II. Five of these eight cells had large  $\theta$ -band membrane potential oscillations and have been called “large  $\theta$  cells” by Domnisoru et al. (2013). Cells without a DAP ( $n = 16$ ) were located in both Layers II and III.

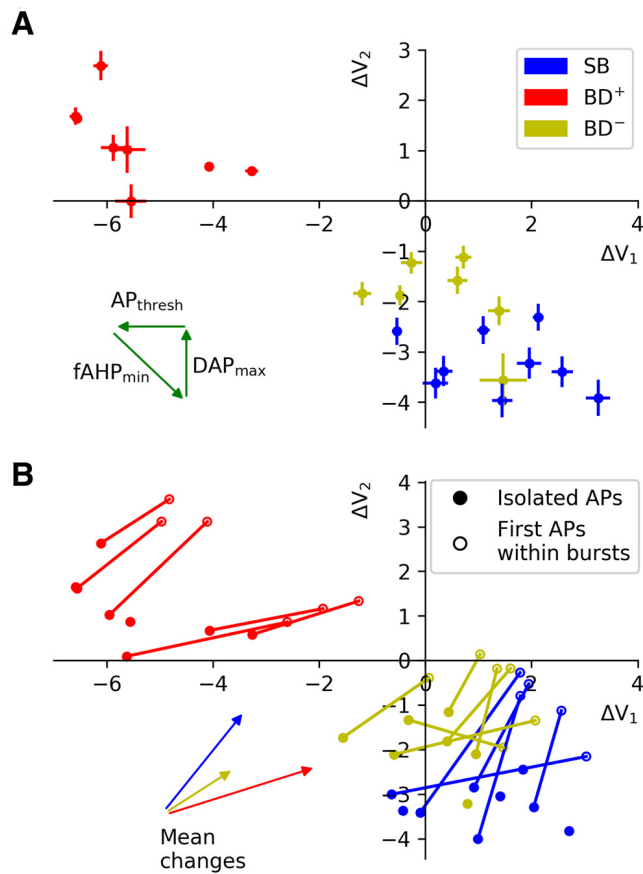


**Figure 2.** Stability of afterpotential parameters. **A**, To quantify the reliability of the parameters characterizing spike afterpotentials, we conducted a bootstrapping analysis, using data from isolated APs. Error bars indicate SEM as obtained from 1000 samples and demonstrate that the fAHP and DAP parameters can be estimated reliably. The three arrows show how a cell's position in the  $\Delta V_1$ – $\Delta V_2$  space changes when the respective parameter is increased. **B**, As an additional test, we computed the parameters  $\Delta V_1$  and  $\Delta V_2$  from voltage traces following the first AP in a burst. With our criteria for APs, this was possible for 17 cells; the other cells are shown as isolated dots. For technical details, see Materials and Methods. For all but two cells, for which  $\Delta V_1$  and  $\Delta V_2$  could be determined for isolated APs and first APs within a burst, both quantities increase when computed from traces within a burst, as can also be seen from the mean changes in each cell class. Importantly, the original grouping in different cell classes is not affected.

### Grid cells differ in their spike-train characteristics

To capture the diversity of spike discharge patterns we conducted a PCA on the spike-time autocorrelations of the 24 intracellularly recorded grid cells (Fig. 3A), as has been done for extracellular recordings (Latuske et al., 2015). We restricted our attention to autocorrelations on short time-scales, in particular to the region between 0 and 50 ms after a spike. We found that the first two principal components, PC1 and PC2, explain 66% and 18% of the cell-to-cell variability, respectively, whereas the contribution from PC3 adds only another 4%. Together, PC1 and PC2 thus account for 84% of the variability. This value changes by <3% when  $\tau_{\max}$  is varied between 30 and 100 ms (data not shown) and starts to decrease for shorter or longer maximal lag. These findings indicate that a 2D PC representation of the grid-cell autocorrelations in the 0- to 50-ms range describes the essence of the cell-to-cell variability.

The mean autocorrelation is highly peaked at a lag  $\tau$  of around 4 ms (Fig. 3B), and so are both principal components (Fig. 3C). This indicates that brief activity bursts in the 250-Hz range play an important role for both the mean grid-cell discharge patterns and their cell-to-cell variability.

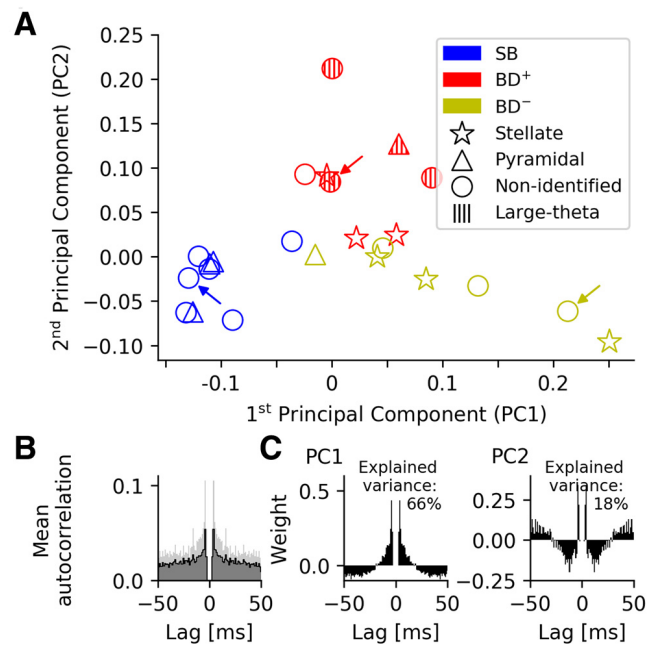


**Figure 3.** Spike-time autocorrelations of MEC grid cells from mice moving in virtual corridors. **A**, visual inspection of spike-time autocorrelations suggests a separation in two major groups, SB and bursting. Based on the intracellular measurements (see Fig. 1), the group of bursting neurons can be subdivided in cells with DAP ( $BD^+$ ), which are shown in red, and cells without detectable DAP ( $BD^-$ ), shown in yellow. The arrows mark the example neurons shown in Figure 1. One cell has intermediate properties and is assigned to the sparsely-bursting group (blue) by k-means clustering ( $k=2$ ). **B**, Mean autocorrelation. Shaded areas show the variability in the data (SD). **C**, The first two principal components of the spike-time autocorrelations. The pronounced peaks in **B**, **C** demonstrate that ISIs of around 4 ms are indicative of both the mean grid-cell discharge patterns and their cell-to-cell variability.

Within this 2D representation (Fig. 3A), neurons without a DAP, shown in blue and yellow, have a negative or only small positive second principal component and strongly vary in their first principal component. Cells with large negative PC1 are SB as the example in the left panel of Figure 1A, whose position in the PC1/PC2 space is marked with a blue arrow in Figure 3A. Cells with positive PC1 burst like the cell in Figure 1A, right panel (Fig. 3A, yellow arrow). Cells with a DAP have positive PC2, only a small PC1, and are also bursting, although with a much broader peak in their autocorrelation as demonstrated by the example in Figure 1A, middle panel (Fig. 3A, red arrow).

This grouping is based on visual inspection of the AC principal components and might not properly distinguish between bursting and sparsely-bursting neurons with small PC1. To better discriminate between these two cell groups, we conducted a k-means clustering with  $k=2$ . The analysis suggested that nine cells should be classified as SB neurons; based on their intracellular characteristics, the remaining 15 bursting (“B”) cells are either DAP cells (“ $BD^+$ ”) or cells without detectable DAP (“ $BD^-$ ”). The same clusters emerge if the spike data from the first and second half of each experiment are treated separately (data not shown), and provide evidence for the robustness of our approach.

All bursty neurons whose anatomic position was classified by Domnisoru et al., are located in Layer II, none in Layer III (two bursty cells were not assigned to a layer). Furthermore, unlike suggested by reports from rats (Ebbesen et al., 2016), bursty neurons are more likely to be stellate than pyramidal cells (six vs two cells), in agreement with the larger abundance of stellate cells compared with pyramidal cells (Alonso and Klink, 1993). There was no detectable difference in the morphology of bursty

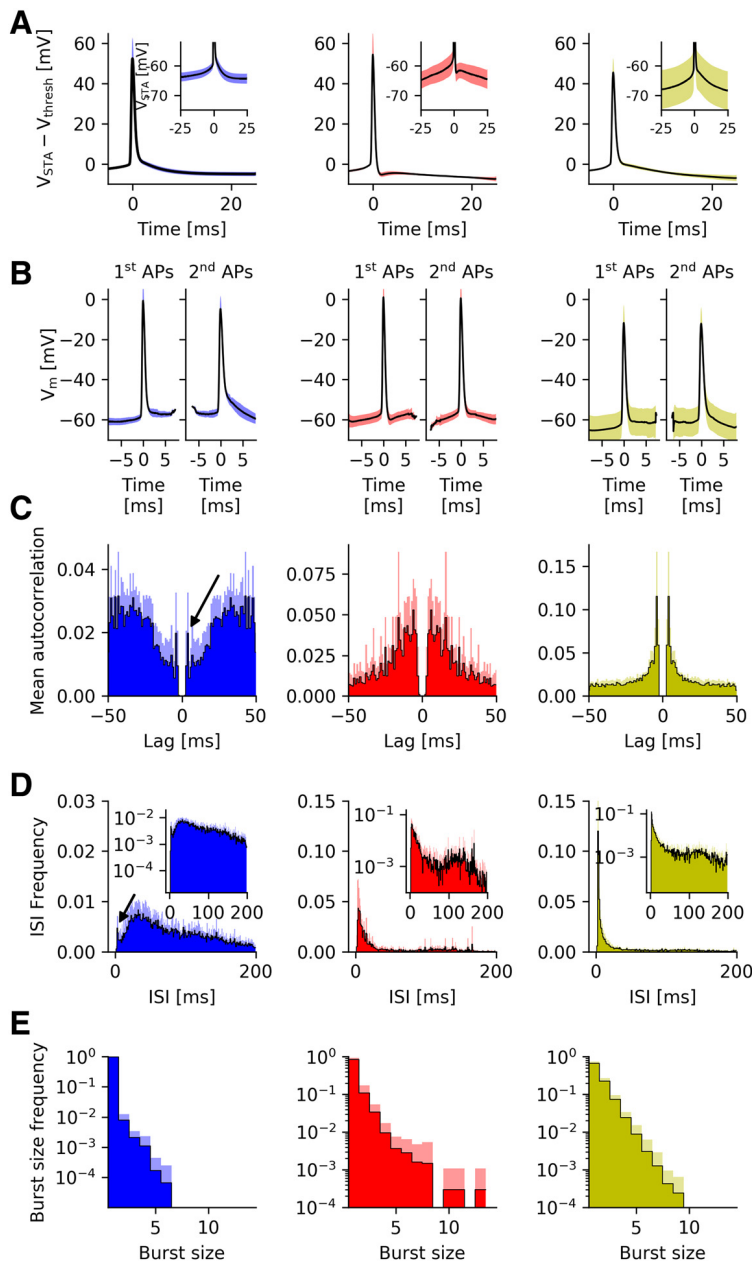


**Figure 4.** Group-level analysis of MEC grid cells from mice moving in virtual corridors. **A**, Population average of the spike-triggered membrane potential for isolated APs (no further AP within 25 ms before and after the AP). The main plot shows data that were aligned to AP onset before the group average was taken, the inset illustrates the absolute membrane potential values. **B**, Population average of spike-triggered membrane potentials for APs within a burst. As in Figure 1C, second APs were clipped when the traces were aligned to the first AP in a burst, and first and third APs were removed when traces were aligned to the second AP in a burst. For details, see Materials and Methods. **C**, Population-averaged autocorrelation functions. **D**, Population-averaged ISIs distributions. Arrows in **B**, **C** highlight bursts of SB cells; inset in **C** with logarithmic time scale emphasizes  $\theta$ -band activity. **E**, Population-averaged intraburst spike count distributions. Shaded areas in all panels, SD.

neurons with and without DAP: Within the BD<sup>+</sup> group ( $n = 8$ ), there were three stellate cells, one pyramidal neuron and four non-identified cells. Within the BD<sup>-</sup> group ( $n = 7$ ), there were three stellate cells, one pyramidal neuron and three non-identified cells. In contrast, not a single non-bursty cell was identified as a stellate cell (pyramidal and non-identified cells: three and six out of  $n = 9$ , respectively) and non-bursty neurons may have a tendency to reside in Layer III (three vs one cell in Layer II; five cells were not classified). Finally, in the  $\Delta V_1$ – $\Delta V_2$  representation (Fig. 1D), BD<sup>-</sup> neurons overlap with SB cells, but tend to have less negative  $\Delta V_2$  values and the  $\Delta V_1$  and  $\Delta V_2$  values within the

group of bursty neurons are correlated with a slope of  $-0.49$  (SE: 0.06). The three groupings are robust, as confirmed by bootstrapping and indicated in Figure 2A, error bars.

### Post-AP dynamics explain the spike-train characteristics of bursty grid cells

After dividing the cells into three groups based on their spike-train autocorrelations and DAP characteristics, we compared the group averages for the grid cells' intracellular voltage traces (Fig. 4). Confirming the impression from individual cells, sparsely-bursting neurons show a smooth and monotone AP down-stroke (Fig. 4A, left panel), bursty cells with DAP exhibit a local voltage minimum followed by repolarization (Fig. 4A, middle panel), and compared with SB cells, bursty cells without DAP tend to have two phases of repolarization: an initial AP downstroke followed abruptly by a slower rate of repolarization, yielding a kink in the voltage traces (Fig. 4A, right panel). Within bursts (Fig. 4B), the characteristic differences between the three cell classes are also apparent, with the voltage trace following the second AP in a burst decreasing more rapidly than the trace following the first AP for SB and BD<sup>-</sup> cells; for BD<sup>+</sup> cells, the second AP in a burst is generally not followed by a DAP, which could be a sign that the DAP mechanism benefits from a longer subthreshold period before the AP.

To visualize these distinct features, the spike-triggered voltage traces were averaged for each neuron and then aligned to the cell's mean voltage at AP onset. Without voltage alignment (see insets), group-to-group differences in membrane potential at the onset of isolated APs are apparent (SB:  $-59.42 \pm 1.22$  mV, BD<sup>+</sup>:  $-57.12 \pm 3.09$  mV, BD<sup>-</sup>:  $-61.40 \pm 6.83$  mV) but not significant [ $p$  (BD<sup>+</sup>, BD<sup>-</sup>) = 0.25;  $p$  (BD<sup>-</sup>, SB) = 0.15;  $p$  (BD<sup>-</sup>, SB) = 0.96, Kruskal–Wallis test], as the AP onset voltage varies throughout the experiment, including for the two groups of bursting neurons. We, therefore, focused on voltage slopes and voltage differences between isolated APs and APs occurring with bursts.

The voltage slope during the last 10 ms before the onset of isolated APs does not differ significantly between BD<sup>+</sup> and BD<sup>-</sup> neurons (BD<sup>+</sup>:  $0.50 \pm 0.03$  mV/ms; BD<sup>-</sup>:  $0.48 \pm 0.08$  mV/ms;  $p = 0.35$ , Kruskal–Wallis test) but does so when bursty and sparsely-bursting neurons are compared (B:  $0.49 \pm 0.06$  mV/ms; SB:  $0.34 \pm 0.05$  mV/ms;  $p = 0.00,015$ , Kruskal–Wallis test). For all cell groups, the second AP in a burst was triggered at a higher voltage than the first AP [SB:  $2.51 \pm 0.57$  mV, BD<sup>+</sup>:  $0.78 \pm 0.72$  mV, BD<sup>-</sup>:  $2.21 \pm 0.54$  mV, with  $p$ (BD<sup>+</sup>, BD<sup>-</sup>) =  $9.8 \times 10^{-3}$ ,  $p$ (BD<sup>+</sup>, SB) =  $3.4 \times 10^{-3}$ ,  $p$ (BD<sup>-</sup>, SB) = 0.85, Kruskal–Wallis

text]. Isolated APs are triggered at voltages slightly lower than those of the first AP in a burst (SB:  $-0.96 \pm 0.60$  mV,  $BD^+$ :  $-0.51 \pm 0.71$  mV,  $BD^-$ :  $-0.36 \pm 0.63$  mV). These values do not differ significantly across the three cell groups [ $p(BD^+, BD^-) = 0.70$ ;  $p(BD^+, SB) = 0.38$ ;  $p(BD^-, SB) = 0.36$ , Kruskal–Wallis test]. Finally, for  $BD^+$  cells, the maximal depolarization reached during the DAP was highly variable; when a second AP was not triggered, the DAP maximum lay  $3.75 \pm 0.63$  mV below the second AP's threshold, when averaged across cells. For each cell, the broad distribution of DAP maxima overlapped with the distribution of thresholds for the second AP, consistent with the hypothesis that DAPs play a role in burst firing of  $BD^+$  cells.

The averaged autocorrelations (Fig. 4C, left panel) and ISIs (Fig. 4D, left panel) of sparsely-bursting cells show that although these neurons rarely generate spike sequences with short ISIs, only 2% of all their ISIs are  $<8$  ms, if they do fire such bursts, there is a pronounced short ISI that is only  $4.30 \pm 0.81$  ms long (Fig. 4C,D, black arrows). Both types of bursty neurons exhibit prominent ISI- and autocorrelation peaks at short time scales (Fig. 4C,D, middle and right panels). Population averages within each group show that the most likely ISI of cells without a DAP is significantly shorter than that of cells with a DAP ( $4.12 \pm 0.12$  vs  $6.96 \pm 3.73$  ms,  $p = 0.01$ , Kruskal–Wallis test); the same is true for the autocorrelation peaks ( $4.13 \pm 0.11$  vs  $9.46 \pm 4.41$  ms,  $p = 0.001$ , Kruskal–Wallis test). These differences are readily explained by the different time courses of the post-spike voltage deflections: The rapid fAHP time course of  $BD^+$  cells strongly reduces the chance that a second AP is fired directly after the first AP, whereas in  $BD^-$  cells the down-stroke of the first AP stops abruptly at depolarized levels, often above the AP threshold (Figs. 1B,C, 4A,B).

In fact, the absence of an fAHP in  $BD^-$  cells separates this group from  $BD^+$  cells. Consistent with this picture, the fAHP increases the refractory period (taking the shortest 10% of the ISIs yields a mean ISI of 3.45 ms in  $BD^-$  vs 5.24 ms in  $BD^+$  cells). When the voltage dynamics are released from the fAHP, the DAP is uncovered, which opens a wide “window of opportunity” for a second AP in  $BD^+$  cells. The resulting ISI distributions are broader for  $BD^+$  cells ( $6.7 \pm 3.27$  ms) compared with  $BD^-$  cells ( $3.66 \pm 0.36$  ms,  $p = 0.01$ , Kruskal–Wallis test). For  $BD^+$  cells, the most likely ISI in a burst mirrors  $\Delta t_{DAP}$ , the time interval between an AP and the succeeding DAP peak [median value 5.1 ms, no difference with most likely ISI according to a median test ( $p = 0.61$ )], which suggests a direct role of the post-AP dynamics in burst behavior.

The intrinsic voltage dynamics alone do not explain why sparsely-bursting cells have much broader ISI distributions (Fig. 4D). Other features correlated with SB behavior, however. All identified SB cells were pyramidal neurons, whereas only one out of four  $BD^-$  cells were pyramidal; four of the five SB cells were in LIII, whereas  $BD^-$  cells were solely found in LII. By contrast, the  $BD^-$  and  $BD^+$  groups were not distinguished by cell-type or the layer in which they were found, which makes it unlikely that anatomic differences can explain the observed variations in the spike trains of bursty neurons.

*In vitro*, stellate cells often produce spike doublets or brief bursts (Alessi et al., 2016). We tested whether spike trains *in vivo* showed similar preferences. For this purpose, we computed the frequency with which cells fired two, three, or more spikes in a burst. The frequency of bursts with exactly  $n$  spikes decreases monotonically with  $n$ , and does so for all three cell groups. Doublets and triplets were not overrepresented (Fig. 4E). In 21 out of the 24 cells, the distribution for  $n$  is consistent with an

exponential distribution ( $\chi^2$  goodness of fit test for the correlation between linear fit and data after logarithmic transformation;  $p > 0.05$ ). There is thus no preferred burst size or “unit of information,” such as a spike doublet or triplet. In the spirit of hippocampal “complex spike bursts” (Ranck, 1973), a grid-cell burst can be regarded as just a sequence of two or more spikes with short ISIs. The exact choice of the cutoff threshold is not critical; qualitatively similar results were obtained using ISI thresholds from 8 ms up to 15 ms (data not shown).

### Spike-train characteristics of bursty cells are largely conserved across 1D and 2D environments

So far, the analysis was based on a relatively small number of neurons recorded in head-fixed animals running in a virtual linear corridor (Domnisoru et al., 2013). To explore whether these data generalize to other experimental conditions, we analyzed a complementary dataset that contained 112 grid cells from mice that foraged at random in a square environment (Latuske et al., 2015). Although these extracellular recordings do not offer direct access to the membrane-potential dynamics, they might still reveal signatures of the different post-AP dynamics. In particular, we expected that grid cells would not only show the versus non-bursty dichotomy described by Latuske et al. (2015), but that there would also be qualitative differences within the bursty subpopulation.

To facilitate the comparison between the two datasets we kept the maximum lag of 50 ms and the 1-ms binning when analyzing spike-time autocorrelations. To minimize observer bias, k-means cluster analyses were performed on the 50-dimensional raw autocorrelations as well as in principal-component spaces with  $N = 2-4$  dimensions. We analyzed the robustness of the k-means clustering results by calculating silhouette scores for each value of  $k$  (Rousseeuw, 1987). Irrespective of the dimensionality  $N$  of the data, separation into three clusters led to the best performance; the clusters hardly changed when using different numbers of principal components. Cluster assignment was stable, regardless of whether the autocorrelations were computed from the first or second half of a cell's spike train: 91.1% of the cells kept their cluster identity (Fig. 5B) from the first to the second half when using  $N = 3$  principal components. To compare these data with the previous results, we again plot the first two principal components against each other (Fig. 5A). The mean autocorrelation (Fig. 5C) closely resembled the one obtained from the virtual-track data (Fig. 3B); and so did the principal components (compare Figs. 5D and 3C), as quantified by their similarity (the scalar product computed for time lags up to 50 ms) of 0.86 for PC1 and 0.63 for PC2 when the two experimental conditions are compared.

There is also a high similarity between the corresponding group-averaged autocorrelations in both datasets (SB cells: 0.93,  $BD^-$  cells: 0.93,  $BD^+$  cells: 0.94; compare Figs. 5E and 4C). This is remarkable as the cluster analysis of the open-field data (Latuske et al., 2015) only reflects the overall structure of the grid-cell autocorrelations and is not informed by intracellular measurements. There is, however, one prominent difference between both datasets. The SB neurons recorded by Latuske et al. (Fig. 5E, left panel) fire hardly any spike within the first few milliseconds (so that the authors named them non-bursty neurons) and their autocorrelation has a pronounced peak at around 15 ms. The autocorrelation function of the SB neurons recorded by Domnisoru et al. (2013; Fig. 4C, left panel) exhibits a local peak at around 4 ms, and grows more slowly, with a local maximum at 30–40 ms. On the other hand, the average autocorrelations of

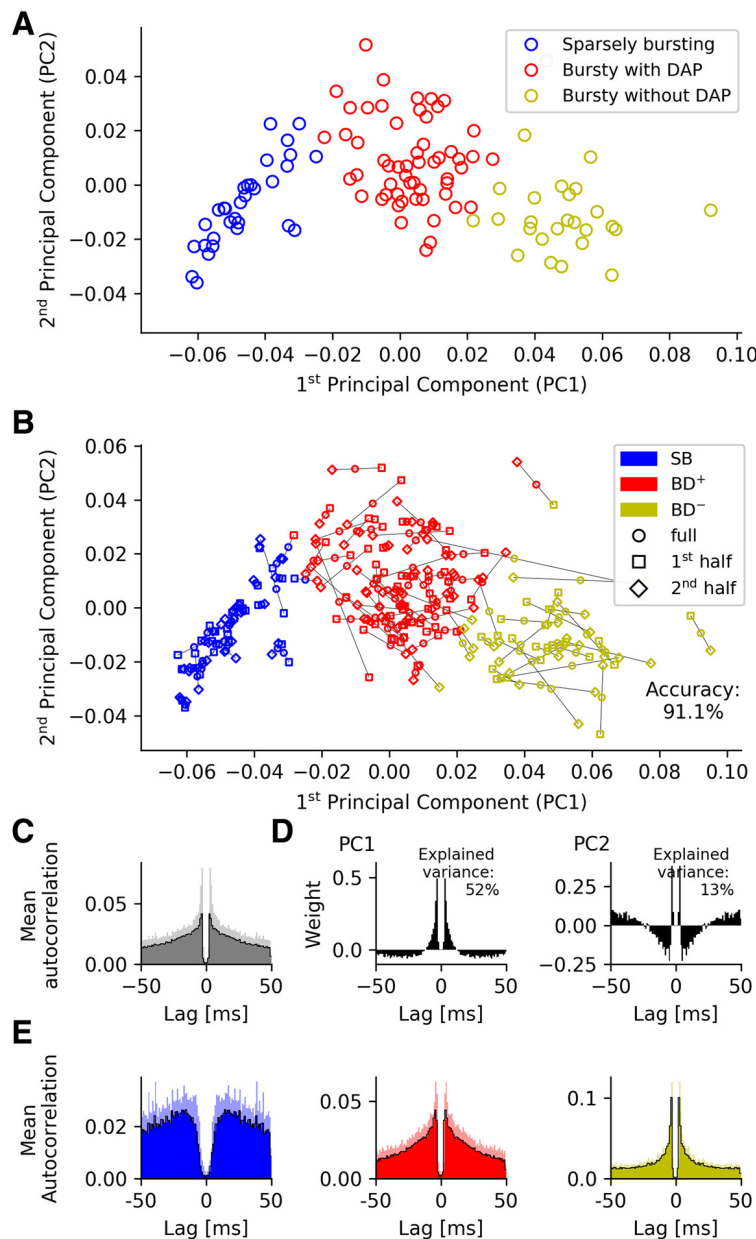


**Figure 5.** Spike-time autocorrelations of MEC grid cells from mice moving in open arenas. **A**,  $k$ -means cluster analysis ( $k = 3$ ) of spike-time autocorrelations. **B**, To test the robustness of the PCA-based class assignment in **A**, we separately considered the first and second half of all spikes for each neuron. We then computed the autocorrelations within these two sets and projected the results into the PC space of the full data.  $k$ -means clustering ( $k = 3$ ) results in only 8.9% of neurons switching group identity, underscoring the robustness of the cluster analysis. **C**, Mean autocorrelation across the grid cells. Shaded areas, SD. **D**, The first two principal components of the spike-time autocorrelations. The sharp peaks in **B**, **C** again demonstrate the prevalence of short ISIs (here around 3.5 ms) in the mean grid-cell discharge patterns as well as their cell-to-cell variability. Shaded areas, SD. **E**, Autocorrelations averaged across all neurons from each cell group reveal a striking similarity between cells recorded on virtual tracks and in open fields. Strongest deviations are shown by non-bursting/SB cells in the Latuske et al. (2015) versus Domnisoru et al. (2013) data.

the  $BD^+$  and  $BD^-$  cells are almost identical when compared across both experimental conditions.

In the virtual-track data, the autocorrelations of the  $BD^-$  neurons ( $n = 7$ ) peak at 4.13 ms with a cell-to-cell variability of 0.11 ms (SD). The autocorrelations of the corresponding cells from the open-field recordings ( $n = 25$ ) have their peak at 3.56 ms (SD: 0.27 ms). The two experimental conditions also differ in the measured grid-field sizes: these are larger in virtual reality than open-field environments (Domnisoru et al., 2013, their supplemental Fig. 9). Consistent with this observation,

other spike-train measures also reflect longer timescales in virtual versus open fields, e.g., the most likely ISI (Fig. 6A), the width of the ISI histogram (Fig. 6B) or the fraction of ISIs below 8 ms (Fig. 6C). Within each experimental setting, however, the three cell groups exhibited the same trends, albeit on slightly different timescales.

Differences between virtual-track and open-field data might be influenced by how spikes are measured intracellularly and extracellularly (Anastassiou et al., 2015). APs of  $BD^-$  neurons tend to slightly increase their width within a burst-like discharge pattern. This implies that the time interval between the peaks of two successive APs (i.e., the intracellularly measured ISI) can be somewhat longer than the time interval between the maximal upstroke slopes of the two APs, a proxy of the extracellularly measured ISI (Henze et al., 2000). Judging from the AP shapes of the  $BD^-$  neurons in the data of Domnisoru et al. (2013), this differential effect is, however, only on the order of 0.1–0.2 ms and thus cannot fully explain the observed timing differences. Other possible factors include differences in the animals' physiological state and stress level in these two highly different experimental conditions. The firing rates (Fig. 6D) are rather similar across experimental conditions and cell groups, which might reflect a general network-level regulation of the average firing rate.

### Spatial response properties are similar across all three grid-cell groups

In the next step of our analysis, we asked whether the pronounced differences between the temporal response characteristics of the three grid-cell groups translate into differences in their spatial firing patterns. The study of Latuske et al. (2015) had shown that this was not the case when one compares bursting with sparsely-bursting grid cells. However, the two groups of bursting neurons might still differ in their spatial behavior. To obtain reliable field estimates, we used the open-field data for this analysis. We tested several measures, including grid score (Sargolini et al., 2006), spatial information (Skaggs et al., 1996), and head-direction score (Sargolini et al., 2006), but could not detect any significant differences between  $BD^+$  and  $BD^-$  cells in these measures (Fig. 6E–G). Only the grid spacing (Hafting et al., 2005) shows a slight trend in that  $BD^-$  cells had a somewhat smaller spacing ( $37.3 \pm 6.6$  cm) than  $BD^+$  cells ( $41.6 \pm 6.9$  cm; Fig. 6H). This finding is in agreement with results by Bant et al. (2020), who report that shorter intraburst ISIs go hand in hand with smaller grid periods. The effect was present, but not strong in the data presented here ( $p = 0.019$ , Kolmogorov–Smirnov test). Differences in grid spacing between bursting and SB cells ( $38.7 \pm 6.3$  cm) were not significant ( $p = 0.98$ , Kolmogorov–Smirnov test).

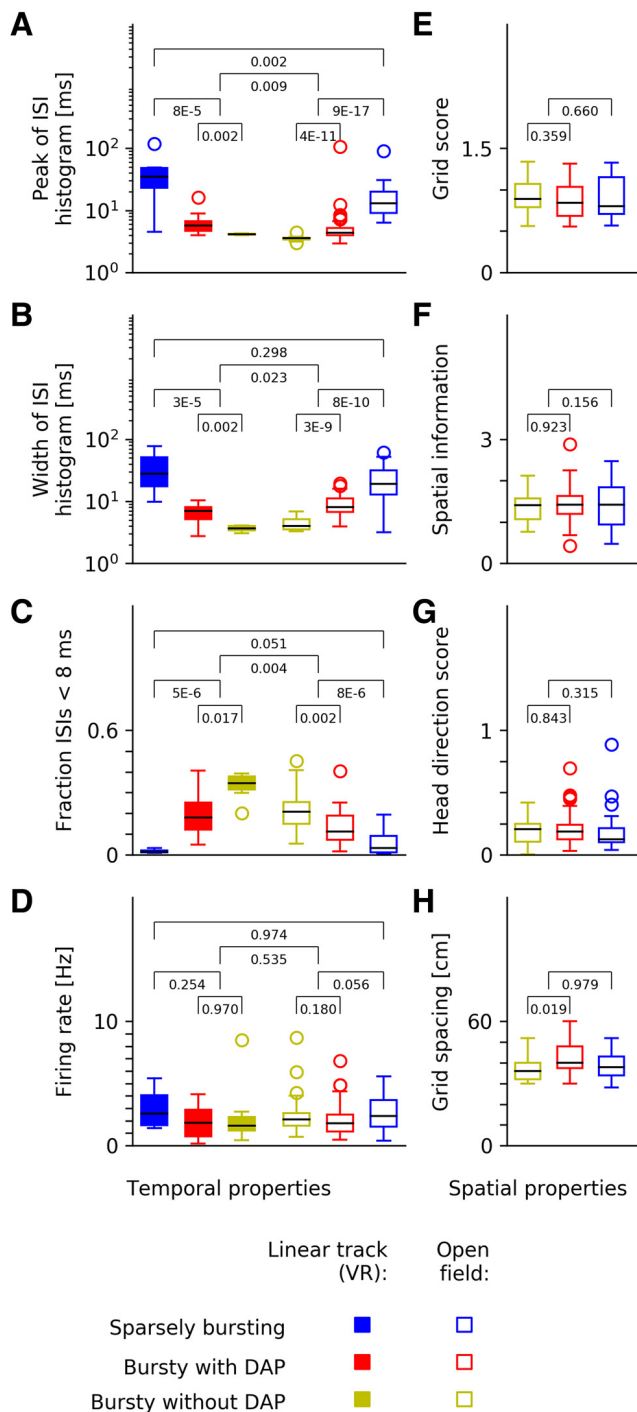


**Figure 6.** Grid-cell spike-train characteristics across datasets and spatial coding. **A–D**, Comparison of linear-track data (filled symbols) and data from the open arena (unfilled symbols). **E–H**, Spatial properties of grid fields recorded in the open arena. **A**, ISI peak, i.e., most likely ISI. **B**, Width of the ISI distribution. **C**, Fraction of ISIs below 8 ms (“burstiness”). **D**, Mean firing rates. **E**, Grid score. **F**, Spatial information. **G**, Head direction score. **H**, Grid spacing. Despite strong differences in temporal spike-train characteristics (**A–C**), mean firing rates (**D**) and spatial coding properties (**E–H**) of grid cells are largely conserved across all three cell groups, with a slight difference in grid spacing between  $BD^+$  and  $BD^-$  cells. The  $p$  values are calculated from Kolmogorov–Smirnov tests.

Slice experiments show that DAPs of stellate cells can be modulated; if the holding potential is decreased, the amplitude  $\Delta V_{DAP}$  of the following DAP increases, and it decreases whenever the holding potential is increased (Alessi et al., 2016). Domnisoru et al. (2013) found that a grid cell depolarizes as the

animal crosses a firing field and hyperpolarizes in the out-of-field regions. Therefore, we wondered whether a  $BD^+$  cell might preferentially generate DAP-mediated bursts on entering a grid field, as the hyperpolarization preceding the membrane-potential ramp might facilitate larger DAPs and thus make DAP-mediated burst firing in these neurons more likely.

To test this hypothesis, we took open-field data from Latuske et al. (2015) and investigated in detail whether spikes belonging to the bursts of a  $BD^+$  cell had an above-chance probability to occur at the edges of its firing fields and, more generally, whether those spikes differed in their spatial statistics from other spikes of the same neuron, in the spirit of a place-cell study by Harris et al. (2001). In particular, we analyzed the distribution of spike distances from the respective firing-field centers as well as topological features of the discharge patterns of  $BD^+$  cells, with special focus on ISIs expected for DAP-triggered bursts. For  $BD^+$  cells, the field-wise mean distance between burst spikes and the respective firing-field center (normalized by each individual firing-field size to range between zero and unity) was  $0.46 \pm 0.10$ , significantly smaller than the same quantity evaluated for isolated spikes ( $0.60 \pm 0.06$ ,  $p = 1.8 \times 10^{-4}$  Kruskal–Wallis test). This shows that burst spikes are far more likely to occur near the firing-field center than isolated spikes and contradicts the hypothesis that burst spikes represent the edges of firing fields. The same was true for  $BD^-$  cells ( $0.44 \pm 0.06$  vs  $0.59 \pm 0.04$ ,  $p = 8.7 \times 10^{-5}$  Kruskal–Wallis test) and SB cells ( $0.46 \pm 0.12$  vs  $0.56 \pm 0.09$ ,  $p = 7.5 \times 10^{-3}$  Kruskal–Wallis test). Compared across the three cell groups, the mean distances for burst spikes were not statistically different (SB vs  $BD^+$ :  $p = 0.99$ , SB vs  $BD^-$ :  $p = 0.85$ ,  $BD^+$  vs  $BD^-$ :  $p = 0.72$ , Kruskal–Wallis test). We thus did not find a special role for bursts in spatial coding. As a complementary check, we used the data from Domnisoru et al. (2013) to search for whether DAP deflections measured in the firing fields of  $BD^+$  cells were smaller than the DAP deflections of out-of-field spikes but did not find any obvious changes either.

These findings suggest that despite the striking differences in the spike-train patterns of bursty cells with and without DAP, these differences have no obvious consequences for the cells’ spatial tuning properties. Temporal variations in the membrane potential, in particular the large  $\theta$  oscillations observed in some bursty grid cells, are uncorrelated with the animal’s trajectory and may easily mask less prominent spatial dependencies. In fact, decoupling of spatial and temporal tuning characteristics might endow the system with added plasticity and computational flexibility.

### Bursty grid cells: one continuum or two clusters?

Since  $BD^+$  and  $BD^-$  cells showed indistinguishable spatial tuning, we reconsidered their partition into two distinct groups based on their temporal firing characteristics. Could it be that the data are better described as a single group with continuously varying parameters?

To answer this question, we went back to the grid-cell data from Domnisoru et al. (2013) and analyzed how the cells’ salient spike-train characteristics depended on the two biophysical parameters  $\Delta V_1$  and  $\Delta V_2$  (Fig. 7). The mean firing rate does not correlate with  $\Delta V_1$  and  $\Delta V_2$  (Fig. 7A,B). There are also no significant dependencies within the  $BD^+$  and  $BD^-$  groups ( $\Delta V_1$ :  $p_{BD^+} = 0.88$ ,  $p_{BD^-} = 0.24$ ;  $\Delta V_2$ :  $p_{BD^+} = 0.58$ ,  $p_{BD^-} = 0.90$ , as tested by independently shuffling the two coordinates of the respective data points and computing the Pearson correlation for each new sample; the  $p$  value is given by the fraction of samples for which the correlation value was larger than in the original sample).



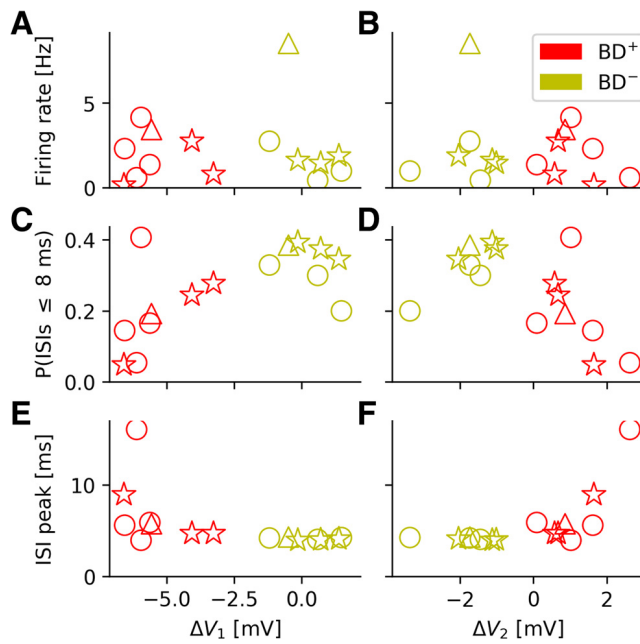


**Figure 7.** Cluster structure of the bursty-grid-cell population. Dependence of key spike-train parameters on the amplitude of fast AHP ( $\Delta V_1$ ) and afterdepolarization ( $\Delta V_2$ ). For a definition of these two parameters, see, e.g., the caption of Figure 1. **A, B**, mean firing rates. **C, D**, Fraction of ISIs below 8 ms (“burstiness”). Across the entire population of bursty neurons, the larger  $\Delta V_1$ , the more frequent are short ISIs. **E, F**, Location of ISI peak. While the firing rates do not exhibit a trend, neither within the two cell groups nor across the groups, the other quantities depicted show trends that differ from the null-hypothesis (no increase/decrease as a function of  $\Delta V_1$  or  $\Delta V_2$ ). The data also suggest that the population of bursty neurons either forms one joint although under-sampled cloud or contains two distinct subpopulations. In either case the spike-train characteristics do depend on the cells’ DAP properties.

A different picture emerges when the fraction of short ISIs (below 8 ms) is considered (Fig. 7C,D). Visual inspection suggests a joint trend for  $BD^+$  and  $BD^-$  cells; the larger  $\Delta V_1$ , the more frequent are short ISIs (Fig. 7C). With a  $p = 0.013$ , this trend is statistically significantly different from the null-hypothesis (no increase/decrease as a function of  $\Delta V_1$ ), and in agreement with our earlier functional interpretation of DAPs: for negative  $\Delta V_1$  (i.e.,  $BD^+$  cells), cells quickly hyperpolarize, making very short ISIs rare.

Consistent with this observation, the location of the ISI peak tends to grow for increasingly negative  $\Delta V_1$  (Fig. 7E) and increasingly positive  $\Delta V_2$  (Fig. 7F) if the entire population of bursty neurons is considered ( $\Delta V_1$ :  $p = 0.04$ ,  $\Delta V_2$ :  $p = 0.01$ ). Within the  $BD^-$  population, however, the ISI peak does hardly vary at all, as emphasized before.

These results indicate that there is no clear-cut answer to the question whether the population of bursty neurons forms one joint although under-sampled cloud or contains two distinct subpopulations. More importantly, however, is the observation that in either case, certain spike-train characteristics do depend on the cells’ individual DAP properties, which supports the view that DAPs do not only exist under *in vivo* conditions but may also play a functional rule.

### Non-grid cells show same DAP and spike-train characteristics as grid cells

In the last step of our analysis, we asked whether non-grid cells differed from grid cells in their DAP behavior or spike-time autocorrelation characteristics. To this end, we first determined

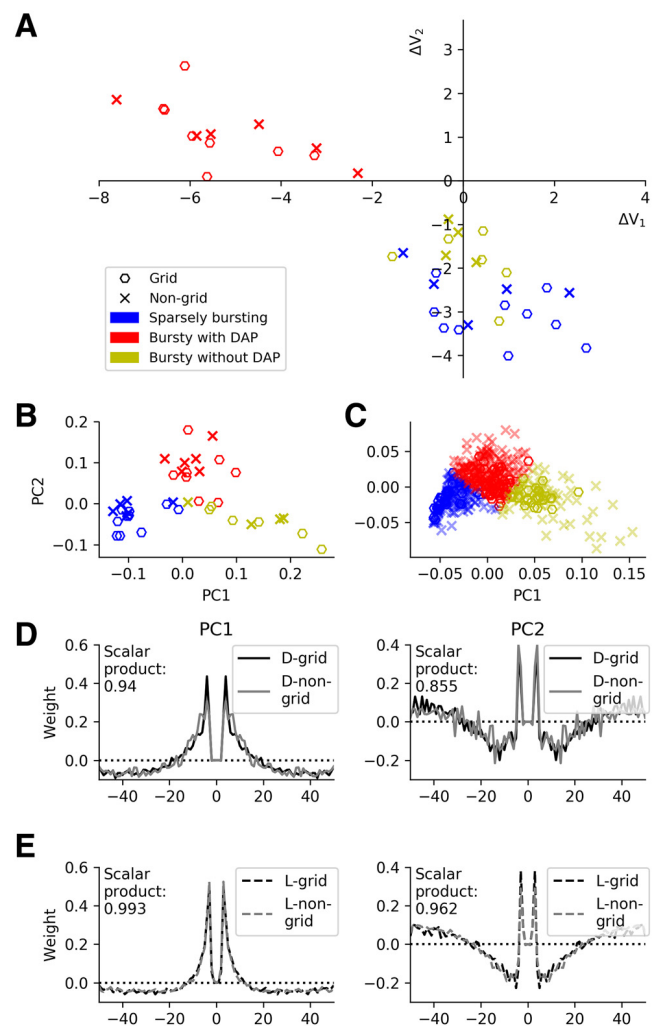


**Figure 8.** Comparison of the characteristics of grid cells and non-grid cells. **A**, Quantification of spike afterpotentials as in Figure 1D but now for all principal cells recorded on the virtual linear track. **B**, PCA of spike-time autocorrelations as in Figure 3A but now for all principal cells recorded on the virtual linear track. **C**, PCA of spike-time autocorrelations as in Figure 5A but now for all principal cells recorded in the open environment. The high similarity between grid cells and non-grid cells suggests that the three functional cell classes identified in this study are universal across all principal cells in the superficial MEC layers. **D**, First and second principal components (left and right panels, respectively) of the virtual-track dataset for grid cells and non-grid cells. The similarity of the PC components is measured by the scalar product for time lags up to 50 ms. **E**, As in **D**, but now for the data recorded in the open environment. The values of the scalar products are rather close to their maximal value of 1 and underscore the similarity of the grid-cell and non-grid-cell autocorrelations and their cluster structure.

the DAP parameters  $\Delta V_1$  and  $\Delta V_2$  for all 40 neurons on linear tracks in virtual reality. As shown in Figure 8A, non-grid cells (represented by “x”) fall into the same data clouds as the grid cells (represented by open hexagons) when these two intracellular measures are considered. Similarly, a PCA of the spike-train autocorrelations of the entire dataset (Fig. 8B) exhibits a 2D structure that is highly reminiscent of that when only grid cells are taken into account (Fig. 3A). The same is true for the PCA of the spike-train autocorrelations of the open-field data from Latuske et al. (2015), shown in Figure 8C. In fact, even the principal components themselves are highly similar when computed for grid cells only or for non-grid cells only (Fig. 8D,E). Moreover, the entire dataset exhibits the same ambiguity concerning the “one versus two clusters” question (Fig. 9) as when only grid cells are considered (Fig. 7).

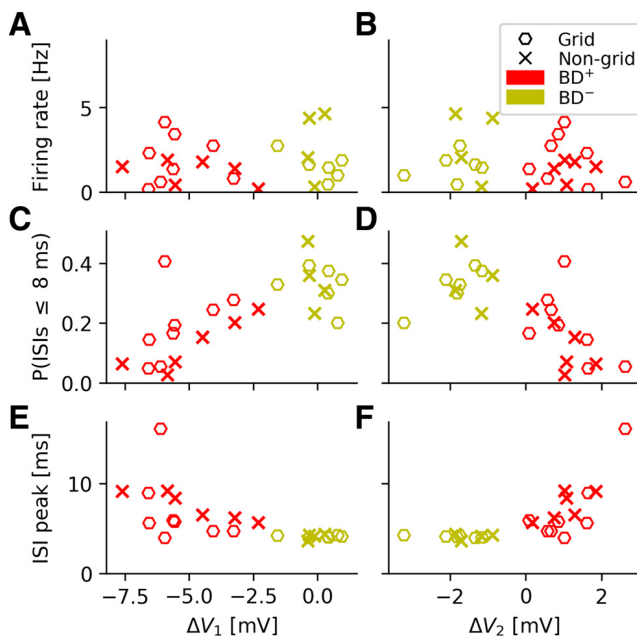


**Figure 9.** Cluster structure of all bursty principal cells recorded in virtual reality. Dependence of key spike-train parameters on fast AHP ( $\Delta V_1$ ) and afterdepolarization ( $\Delta V_2$ ). **A, B**, Mean firing rates. **C, D**, Fraction of ISIs below 8 ms (“burstiness”). **E, F**, Location of ISI peak. There is no apparent difference to the grid-cell cluster structure shown in Figure 7.

Consistent with this observation, the remarkably small cell-to-cell variability in the autocorrelation peaks of  $BD^-$  grid cells (virtual linear track:  $4.13 \pm 0.11$  ms; open field:  $3.56 \pm 0.27$  ms) is also shared by the non-grid  $BD^-$  cells (virtual linear track:  $4.05 \pm 0.25$  ms, open field:  $3.67 \pm 0.60$  ms), and these peaks are significantly shorter than the autocorrelation peaks of the non-grid  $BD^+$  cells (virtual linear track:  $9.29 \pm 3.53$  ms,  $p = 0.02$ , Kruskal–Wallis test; open field:  $6.99 \pm 3.52$  ms,  $p = 1.15 \times 10^{-29}$ , Kruskal–Wallis test). All data: mean values  $\pm$  SD. The SD describes the cell-to-cell variability.

Taken together, our findings demonstrate not only that the DAP characteristics of grid cells have no consequences for their spatial firing properties (Fig. 6E–G) but that in addition, non-grid cells and grid cells fall into the same three subgroups, SB neurons, bursty with DAP and bursty without DAP. Both results suggest that DAPs and burst firing are not critical for spatial navigation.

## Discussion

Tetrode recordings in freely moving rats (Mizuseki et al., 2009; Ebbesen et al., 2016) and mice (Latuske et al., 2015) have shown that principal neurons in superficial MEC layers come in two functional subclasses, cells that burst frequently and others that do not or only rarely burst. Our analysis of whole-cell data from mice running on linear virtual tracks (Domnisoru et al., 2013) suggests that principal cells located in Layer III tend to be SB and that they do not generate DAPs, in agreement with previous slice studies in rats (Canto and Witter, 2012).

Bursty neurons varied strongly in the overall shape of their autocorrelations (as shown for grid cells in Fig. 4C) and their ISI distributions (Fig. 4D). This diversity can be understood in terms of the cell-specific shapes of spike afterpotentials: Neurons without a DAP ( $BD^-$  cells) had ISI distributions that peaked sharply at around 4 ms and varied only minimally across that group of cells whereas the ISIs of neurons with a DAP ( $BD^+$  cells) were most frequent between 5 and 15 ms.

At first sight, the gap between  $BD^+$  and  $BD^-$  cells in the  $\Delta V_1$ – $\Delta V_2$  diagram (Fig. 1D) speaks against a continuum of bursty grid cells and rather points to the existence of two separate subgroups. This impression might, however, be due to a sampling artifact; there are only 15 such cells with intracellular recordings in the dataset from Domnisoru et al. (2013). We, therefore, investigated the dependencies of various spike-train characteristics on  $\Delta V_1$  and  $\Delta V_2$  (Fig. 7). The smooth behavior of some measures, such as the burstiness, i.e., the fraction of ISIs below 8 ms, or the ISI-peak location, and the lack of any sharp transitions in the other measures, support the characterization of the  $BD^+$  and  $BD^-$  grid-cell subgroups as a single, although sparsely populated group that spans a range of properties. The  $BD^+$  and  $BD^-$  grid-cell subgroups have a roughly equal stellate-to-pyramidal-cell ratio (3:1), which means that cellular morphology is not indicative of the cell’s type of bursting behavior. Moreover, the bursting behavior of non-grid cells is almost identical (Fig. 8A) to grid cells (see also Fig. 8D,E), so the spatial encoding properties of neurons are also not an indicator of their bursting behavior.

Consistent with the hypothesis of one single group of bursty neurons, the physiological properties of individual cells could either be fixed or undergo plastic changes that move the biophysical cell parameters between the  $BD^+$  and  $BD^-$  regions. In the  $\Delta V_1$ – $\Delta V_2$  space (Figs. 1D, 8A), a transition from  $BD^+$  to  $BD^-$  corresponds to an increase in  $\Delta V_1$  accompanied by a somewhat smaller decrease in  $\Delta V_2$ . Such a parameter change can be achieved through modifications of the AP-threshold, fAHP minimum and/or DAP maximum, as illustrated by the arrows in Figure 2A. Various ion channels have been implicated in DAP generation, from sodium and calcium channels (Alessi et al., 2016), to potassium (Eder et al., 1991) and HCN channels (Dickson et al., 2000), which also play a key role for slower grid-cell rhythms (Giocomo and Hasselmo, 2009). These channels could be regulated, e.g., by cholinergic stimulation, which has been shown to induce DAPs and after discharges in MEC-Layer-II neurons (Magistretti et al., 2004). Such modulations would have a direct impact on the precise temporal characteristics of bursting neurons. In addition, cells with  $BD^-$  characteristics and thus shorter intraburst ISIs seem to have smaller grid spacing than  $BD^+$  cells, in accordance with findings by Bant et al. (2020), although the significance of our results is weak.

Modulations of the biophysical parameters governing the afterpotentials might even occur at the time scale of single runs through the animal’s environment. Indeed, close inspection of individual membrane-potential traces suggests that  $BD^+$  cells do not generate a DAP after every AP; conversely, some APs of  $BD^-$  cells are followed by a DAP. One might even speculate that most bursty cells are capable of generating DAPs, slice experiments in rats suggest 85% of Layer-II stellate cells and 73% of Layer-II pyramids have DAPs (Canto and Witter, 2012), but that this mechanism is under external control so as to switch cells between  $BD^+$  and  $BD^-$  behavior.

Remarkably, the ISI distributions of  $BD^-$  cells have ultra-sharp peaks, whose location varies only minimally within that group. Notably, the same short ISIs are shown by the SB neurons in Layer III (see also Mizuseki et al., 2009) and could be elicited if Layer-III SB neurons received (convergent) synaptic input from Layer-II  $BD^-$  cells. The precise function of burst sequences in the 250- to 300-Hz regime remains an open question. Similarly, it is not obvious how cells with highly distinct firing characteristics can be orchestrated to create one joint grid-cell network (but see Pastoll et al., 2013), in which the SB,  $BD^-$ , and

$BD^+$  cell classes have roughly the same grid score, spatial information and head direction score (Fig. 5E–G). With their high rate of bursts,  $BD^-$  neurons might be ideally suited to drive other neurons in the network, whereas the DAPs of  $BD^+$  cells might trigger synaptic plasticity, similar to their function in CA3 pyramidal neurons (Mishra et al., 2016), and thus play a critical role for network reconfiguration when the animal learns about new environments (Krupic et al., 2018) or goals (Boccaro et al., 2019).

Switching on the DAP mechanism (without interfering with the preceding fAHP) would then increase the probability of additional APs (Alessi et al., 2016) as well as provide a trace for the long-term potentiation of incoming synapses (Mishra et al., 2016). Once these synapses are strengthened and the DAP mechanism has been turned off again (or masked), the cell can fire precisely tuned bursts with short ISIs. These cell-intrinsic processes could be complemented by precisely wired and timed synaptic inputs (Varga et al., 2010; Couey et al., 2013; Pastoll et al., 2013; Buetfering et al., 2014; Fuchs et al., 2016; Schmidt et al., 2017; Winterer et al., 2017). Through short-term plasticity and integrative postsynaptic processes (Lisman, 1997; Izhikevich et al., 2003) such reorganization could result in a stronger influence on downstream neurons.

In contrast to what one might have expected, the strong dependence of DAPs on the neuron's recent history (Alonso and Klink, 1993; Canto and Witter, 2012; Alessi et al., 2016) does not seem to translate into a spatial burst code. For example, one might have hypothesized that the DAP of a Layer-II stellate cell should be particularly large when the animal is moving into one of the cell's firing fields, as this corresponds to raising the membrane potential from its previous out-of-field hyperpolarization. However, we could not find any signature for the ring-like burst-field structure expected in this scenario. In fact, we could not find any nontrivial spatial dependencies despite vigorous search. This came as a surprise, given the role of burst firing for spatial coding in the hippocampus (Harris et al., 2001) or subiculum (Simonnet and Brecht, 2019). Similarly, spike doublets do not seem to play any special role for burst coding. Together, these findings suggest that grid-cell bursts are either not used for spatial coding, apart from their contribution to  $\theta$ -phase precession (Hafting et al., 2008; Reifenstein et al., 2012), or that the spatial coding is masked by temporal fluctuations that are uncorrelated with spatial coordinates.

It is well known that after-spike potentials play a critical role in the control of AP firing patterns. For example, mAHPs control  $\theta$ -band clustering of APs in MEC stellate neurons (Fransén et al., 2004). Our study extends these and related findings to the 250- to 300-Hz range and provides a novel mechanistic explanation of MEC burst firing. Given the inherent limitations of head-fixed virtual reality experiments, whole-cell recordings from rotationally unconstrained animals, such as performed by Chen et al. (2019), should provide further insight into the mechanisms underlying burst phenomena in rodent MEC.

**Acknowledgements:** We thank D. W. Tank and K. Allen for making data from Domnisoru et al. (2013) and Latuske et al. (2015), respectively, available; K. Thurley for support in statistical analysis; and K. Allen, C. Domnisoru, and S. Häusler for stimulating discussions and helpful feedback on the manuscript.

## References

Alessi C, Raspanti A, Magistretti J (2016) Two distinct types of depolarizing afterpotentials are differentially expressed in stellate and pyramidal-like neurons of entorhinal-cortex layer II. *Hippocampus* 26:380–404.

- Alonso A, Klink R (1993) Differential electroresponsiveness of stellate and pyramidal-like cells of medial entorhinal cortex layer II. *J Neurophysiol* 70:128–143.
- Anastassiou CA, Perin R, Buzsáki G, Markram H, Koch C (2015) Cell type- and activity-dependent extracellular correlates of intracellular spiking. *J Neurophysiol* 114:608–625.
- Bant JS, Hardcastle K, Ocko SA, Giocomo LM (2020) Topography in the bursting dynamics of entorhinal neurons. *Cell Rep* 30:2349–2359.
- Boccaro CN, Nardin M, Stella F, O'Neill J, Csicsvari J (2019) The entorhinal cognitive map is attracted to goals. *Science* 363:1443–1447.
- Buetfering C, Allen K, Monyer H (2014) Parvalbumin interneurons provide grid cell-driven recurrent inhibition in the medial entorhinal cortex. *Nat Neurosci* 17:710–718.
- Canto CB, Witter MP (2012) Cellular properties of principal neurons in the rat entorhinal cortex. II. The medial entorhinal cortex. *Hippocampus* 22:1277–1299.
- Chen G, Lu Y, King JA, Cacucci F, Burgess N (2019) Differential influences of environment and self-motion on place and grid cell firing. *Nat Commun* 10:630.
- Chrobak JJ, Buzsáki G (1998) Gamma oscillations in the entorhinal cortex of the freely behaving rat. *J Neurosci* 18:388–398.
- Colgin LL, Denninger T, Fyhn M, Hafting T, Bonnevie T, Jensen O, Moser MB, Moser EI (2009) Frequency of gamma oscillations routes flow of information in the hippocampus. *Nature* 462:353–357.
- Couey JJ, Witoelar A, Zhang SJ, Zheng K, Ye J, Dunn B, Czajkowski R, Moser MB, Moser EI, Roudi Y, Witter MP (2013) Recurrent inhibitory circuitry as a mechanism for grid formation. *Nat Neurosci* 16:318–324.
- Dickson CT, Magistretti J, Shalinsky MH, Fransén E, Hasselmo ME, Alonso A (2000) Properties and role of  $I_h$  in the pacing of subthreshold oscillations in entorhinal cortex layer II neurons. *J Neurophysiol* 83:2562–2579.
- Domnisoru C, Kinkhabwala AA, Tank DW (2013) Membrane potential dynamics of grid cells. *Nature* 495:199–204.
- Ebbesen CL, Reifenstein ET, Tang Q, Burgalossi A, Ray S, Schreiber S, Kempter R, Brecht M (2016) Cell type-specific differences in spike timing and spike shape in the rat parasubiculum and superficial medial entorhinal cortex. *Cell Rep* 16:1005–1011.
- Eder C, Ficker E, Gundel J, Heinemann U (1991) Outward currents in rat entorhinal cortex stellate cells studied with conventional and perforated patch recordings. *Eur J Neurosci* 3:1271–1280.
- Engel TA, Schimansky-Geier L, Herz AVM, Schreiber S, Erchova I (2008) Subthreshold membrane-potential resonances shape spike-train patterns in the entorhinal cortex. *J Neurophysiol* 100:1576–1589.
- Fransén E, Alonso AA, Dickson CT, Magistretti J, Hasselmo ME (2004) Ionic mechanisms in the generation of subthreshold oscillations and action potential clustering in entorhinal layer II stellate neurons. *Hippocampus* 14:368–384.
- Fuchs EC, Neitz A, Pinna R, Melzer S, Caputi A, Monyer H (2016) Local and distant input controlling excitation in layer II of the medial entorhinal cortex. *Neuron* 89:194–208.
- Giocomo LM, Hasselmo ME (2009) Knock-out of HCN1 subunit flattens dorsal-ventral frequency gradient of medial entorhinal neurons in adult mice. *J Neurosci* 29:7625–7630.
- Hafting T, Fyhn M, Bonnevie T, Moser M-B, Moser EI (2008) Hippocampus-independent phase precession in entorhinal grid cells.
- Hafting T, Fyhn M, Molden S, Moser M-B, Moser EI (2005) Microstructure of a spatial map in the entorhinal cortex. *Nature* 436:801–806.
- Harris KD, Hirase H, Leinekugel X, Henze DA, Buzsáki G (2001) Temporal interaction between single spikes and complex spike bursts in hippocampal pyramidal cells. *Neuron* 32:141–149.
- Hasselmo ME (2014) Neuronal rebound spiking, resonance frequency and theta cycle skipping may contribute to grid cell firing in medial entorhinal cortex. *Philos Trans R Soc Lond B Biol Sci* 369:20120523.
- Henze DA, Borhegyi Z, Csicsvari J, Mamiya A, Harris KA, Buzsáki G (2000) Intracellular features predicted by extracellular recordings in the hippocampus in vivo. *J Neurophysiol* 84:390–400.
- Izhikevich EM, Desai NS, Walcott EC, Hoppensteadt FC (2003) Bursts as a unit of neural information: selective communication via resonance. *Trends Neurosci* 26:161–167.
- Krupic J, Bauza M, Burton S, O'Keefe J (2018) Local transformations of the hippocampal cognitive map. *Science* 359:1143–1146.

- Latuske P, Toader O, Allen K (2015) Interspike intervals reveal functionally distinct cell populations in the medial entorhinal cortex. *J Neurosci* 35:10963–10976.
- Lisman JE (1997) Bursts as a unit of neural information: making unreliable synapses reliable. *Trends Neurosci* 20:38–43.
- Magistretti J, Ma L, Shalinsky MH, Lin W, Klink R, Alonso A (2004) Spike patterning by  $Ca^{2+}$ -dependent regulation of a muscarinic cation current in entorhinal cortex layer II neurons. *J Neurophysiol* 92:1644–1657.
- Mishra RK, Kim S, Guzman SJ, Jonas P (2016) Symmetric spike timing-dependent plasticity at CA3–CA3 synapses optimizes storage and recall in autoassociative networks. *Nat Commun* 7:11552.
- Mizuseki K, Sirota A, Pastalkova E, Buzsáki G (2009) Theta oscillations provide temporal windows for local circuit computation in the entorhinal-hippocampal loop. *Neuron* 64:267–280.
- Newman EL, Hasselmo ME (2014) Grid cell firing properties vary as a function of theta phase locking preferences in the rat medial entorhinal cortex. *Front Syst Neurosci* 8:193.
- Pastoll H, Solanka L, van Rossum MC, Nolan MF (2013) Feedback inhibition enables  $\theta$ -nested  $\gamma$  oscillations and grid firing fields. *Neuron* 77:141–154.
- Pedregosa F, Varoquaux G, Gramfort A, Michel V, Thirion B, Grisel O, Blondel M, Prettenhofer P, Weiss R, Dubourg V, VanderPlas J, Passos A, Cournapeau D, Brucher M, Perrot M, Duchesnay V (2011) Scikit-learn: machine learning in Python. *J Mach Learn Res* 12:2825–2830.
- Ranck JBJ (1973) Studies on single neurons in dorsal hippocampal formation and septum in unrestrained rats. I. Behavioral correlates and firing repertoires. *Exp Neurol* 41:461–531.
- Reifenstein ET, Kempter R, Schreiber S, Stemmler MB, Herz AVM (2012) Grid cells in rat entorhinal cortex encode physical space with independent firing fields and phase precession at the single-trial level. *Proc Natl Acad Sci USA* 109:6301–6306.
- Rousseeuw PJ (1987) Silhouettes: a graphical aid to the interpretation and validation of cluster analysis. *Comput Appl Math* 20:53–65.
- Sargolini F, Fyhn M, Hafting T, McNaughton BL, Witter MP, Moser M-B, Moser EI (2006) Conjunctive representation of position, direction, and velocity in entorhinal cortex. *Science* 312:758–762.
- Schmidt H, Gour A, Straehle J, Boergens KM, Brecht M, Helmstaedter M (2017) Axonal synapse sorting in medial entorhinal cortex. *Nature* 549:469–475.
- Schmidt-Hieber C, Häusser M (2013) Cellular mechanisms of spatial navigation in the medial entorhinal cortex. *Nat Neurosci* 16:325–331.
- Simonnet J, Brecht M (2019) Burst firing and spatial coding in subicular principal cells. *J Neurosci* 39:3651–3662.
- Skaggs WE, McNaughton BL, Wilson MA, Barnes CA (1996) Theta phase precession in hippocampal neuronal populations and the compression of temporal sequences. *Hippocampus* 6:149–172.
- Varga C, Lee SY, Soltesz I (2010) Target-selective GABAergic control of entorhinal cortex output. *Nat Neurosci* 13:822–824.
- Virtanen P, Gommers R, Oliphant TE, Haberland M, Reddy T, Cournapeau D, Burovski E, Peterson P, Weckesser W, Bright J, van der Walt SJ, Brett M, Wilson J, Millman KJ, Mayorov N, Nelson ARJ, Jones E, Kern R, Larson E, Carey CJ, et al. (2020) SciPy 1.0: fundamental algorithms for scientific computing in Python. *Nat Methods* 17:261–272.
- Winterer J, Maier N, Wozny C, Beed P, Breustedt J, Evangelista R, Peng Y, D’Albis T, Kempter R, Schmitz D (2017) Excitatory microcircuits within superficial layers of the medial entorhinal cortex. *Cell Rep* 19:1110–1116.

## 4 Second Manuscript

# Grid cells anticipate the animal's future movement

Dóra Éva Csordás<sup>1,2</sup>, Johannes Nagele<sup>1,2</sup>, Martin Stemmler<sup>1,2</sup>, Andreas V. M. Herz<sup>1,2</sup>

*1. Bernstein Center for Computational Neuroscience Munich and Faculty of Biology, Ludwig-Maximilians-Universität München, Großhaderner Straße 2, 82152 Martinsried-Planegg, Germany*

*2. Graduate School of Systemic Neurosciences, Ludwig-Maximilians-Universität München, Großhaderner Straße 2, 82152 Martinsried-Planegg, Germany*

## *Abstract*

Grid cells in the rodent medial entorhinal cortex preferentially fire spikes when the animal is within certain regions of space. When experimental data are averaged over time, spatial firing fields become apparent. If these firing fields represented only the current position of the animal, a grid cell's firing should not depend on whether the animal is running into or out of a firing field. Yet many grid cells are sensitive to the animal's direction of motion relative to the firing-field center. Such apparent egocentric "inbound-outbound tuning" could be a sign of prospective encoding of future position, but it is unclear whether grid cells code ahead in space or in time. To investigate this question, we decided to undo the inbound-outbound modulation by shifting all spikes within a given firing field by a fixed distance in space or in time. For grid-cell data recorded in mice, optimizing in space requires a forward shift of around 2.5 cm, whereas optimizing in time yielded a forward shift of about 170 ms. In either case the firing-field sizes decrease. Minimizing just the field size yields somewhat smaller shifts (roughly 1.8 cm and around 115 ms ahead). Jointly optimizing along the temporal and spatial dimension reveals a continuum of flat inbound-outbound tuning curves and a shallow minimum for field sizes, located at about 2.3 cm and 35 ms. These findings call into question a purely spatial or purely temporal interpretation of grid-cell firing fields and inbound-outbound tuning.

Author contributions: All authors designed research. DÉC performed research and analyzed data. DÉC and AVMH wrote and edited the paper with support from JN and MS.

Conflict of Interest: The authors declare no competing financial interests.

*This work was supported by the German Federal Ministry for Education and Research Grant 01GQ0440. We thank K. Allen for making data from Latuske et al. (2015), available; S. Häusler for stimulating discussions and helpful feedback on the manuscript.*

## *Introduction*

Navigating through space requires a well-organized network of spatially active cells, such as place cells in the hippocampus (O'Keefe et al., 1971), head-direction cells in the postsubiculum (Taube et al., 1990), grid cells in the medial entorhinal cortex (Hafting et al., 2005), boundary vector cells in the subiculum (Lever et al., 2009) and speed cells in the medial entorhinal cortex (Kropff et al., 2015).

The traditional working hypothesis that these cells encode the current values of the dynamic variables they are tuned to, was already shown to be incorrect. Head direction cells, for example, anticipate future head directions by up to 95 ms (Stackman and Taube, 1998), and place and grid cells anticipate future spatial locations by 30-120 ms (Muller and Kubie, 1989, Sharp 1999) and 50-80 ms (Kropff et al., 2015), respectively. In addition, the cells' coding properties, as inferred from the experimental data, may reflect implicit assumptions about the neural code. In fact, Huxter et al. (2008) showed that shifting the measured spike positions forward along the movement direction can shrink the calculated place field size. As a consequence, the calculated anticipatory activity of spatially tuned cells is influenced by the experimentalist's choice about where to place the tracking LEDs on the animal's head – the chosen LED position may or may not reflect the "true" position perceived by the animal.

To disentangle spatial effects from temporal anticipation, considering velocity-dependencies might help. This approach has proven successful in other studies and showed that head-direction cells in the anterodorsal nucleus and in the lateral mammillary nuclei systematically shift their directional firing preference as a function of angular velocity (Blair and Sharp, 1995, Stackman and Taube, 1998). Place cell firing correlates with future locations at slow speeds, but at high speeds it correlates with past locations (Sharp, 1999). Studying anticipation in animals foraging in 2D or 3D comes with an added benefit compared to 1D movements in that spatial and temporal aspects decouple as soon as the animal moves on a curved path.



It has remained an open question whether place cells or grid cells indeed show true anticipation or whether the observed phenomena are just a side effect of incorrectly assigning the animal's perceived position on the body. Focusing on the medial entorhinal cortex, the present study explores whether the spatial position shifts, temporal anticipation or possibly a combination of both scenarios best explain grid cell firing.

## *Materials and Methods*

### **Data**

We analyzed data reported in Latuske et al. (2015). The dataset contained tetrode data (Sampling rate: 20 or 24 kHz) obtained from male mice during movements in a square arena (70 x 70 cm). The trajectory was recorded by three LEDs placed on the head of the animal, two at the ears, and one centrally positioned close to the animal's neck. The spatial position of the animal was defined as the midpoint between the two LEDs at the ears (as shown in Fig. 1A). The head direction was determined by the vector pointing from the neck LED to this midpoint.

### **Grid cell selection**

After removing recording sessions for which the animal trajectories showed artifacts, 522 principal cells were identified using the same criteria as in Latuske et al. (2015); in particular, the mean firing rate had to be smaller than 10 Hz. Out of those cells, 115 cells had been classified as grid cells by Latuske et al..

### **Grid field detection**

The spikes belonging to each grid field ("member spikes") and the associated grid-field centers were assigned using the Mean Shift algorithm (Comaniciu and Meer, 2002). The Mean Shift algorithm and the estimation of its bandwidth (number of samples = 10) was performed using the Python implementation from the `sklearn.cluster` package (using default parameters otherwise). To account for temporal effects, each spike data was weighted by the dwell time of the animal in the corresponding spatial bin (2x2 cm) before clustering. The radius of a grid field was computed as the maximal distance of the member spikes from the respective grid field center. To avoid boundary effects, we focused on well-defined grid fields away from the arena's boundary. To this end, grid fields were only considered further if the disk drawn around the grid-field center with the field radius was fully within the arena. Based on these criteria, 45 grid cells with 55 grid fields were included in the study (for 36 grid cells with 44 grid fields, the head direction was also recorded).

## Inbound-outbound firing probability in a grid field

To compute inbound-outbound firing probabilities, every spike in a given grid field was assigned an angle  $\alpha$  which was the angle between the momentary velocity vector and the vector pointing from the spike position to the grid field center (see Fig. 1A). With this convention,  $0^\circ$  means that the animal was heading directly towards the grid field center when the spike was generated and  $\pm 180^\circ$  means that the grid field center was straight behind the animal. Furthermore, a positive angle means that the grid field center was on the left side of the animal and a negative angle means that it was on the animal's right side. Accordingly, if  $\alpha$  was between  $-90^\circ$  and  $90^\circ$  the spike was fired on a trajectory segment on which the animal moved closer to the firing-field center and which will be called an "inbound trajectory", otherwise, the animal moved on an "outbound trajectory". The trajectory points themselves were assigned an angle in the same way. Polar histograms with 36 ten-degree bins in the range of  $-180^\circ$  to  $180^\circ$  of both the spikes and the trajectory points were computed. The inbound-outbound firing rate was defined as follows:

$$Firing\ rate_{inbound-outbound}(\alpha) = \frac{Histogram_{spike}(\alpha)}{Histogram_{trajectory}(\alpha)} \cdot sampling\ rate$$

To correct for different firing rates in the grid fields, firing probabilities, whose sum over angular bins equals unity, were calculated by normalizing the firing rates.

## Inbound-outbound tuning in a grid field

The firing probability curves were fit by the least squares method with the following cosine model:

$$cosine\ fit(\alpha) = \frac{1}{NB} + \frac{MA}{NB} \cos(\alpha - offset)$$

where NB was the number of bins (36) and the free parameters were the angular offset and the modulation amplitude (MA), which was assumed to be positive or zero. From the MA and offset we computed two related measures, i.e. the modulation index (MI) and the peak phase. If the peak of the cosine fit was between  $-90^\circ$  and  $90^\circ$  the MI was defined to be equal to the absolute value of MA, otherwise MI was set to minus the absolute value of MA. The peak phase was the center of the

bin at which the cosine fit had its maximum value. With these definitions, both the MI and the peak phase carry information about a grid cell was inbound or outbound tuned for the grid field under consideration (Fig. 1B).

### **Statistical validation of a grid field being inbound-outbound tuned**

To decide whether a grid field is significantly tuned we shuffled the bins of the original firing probability curve of the grid field 10000 times and fitted each shuffle again with the cosine model. If the grid field's MI was smaller than the 5<sup>th</sup> percentile or higher than the 95<sup>th</sup> of the shuffled MI distribution, then the field was called significantly tuned. 42 out of 55 grid fields were significantly tuned. If the peak phase was less than  $\pm 45^\circ$  away from  $0^\circ$  or  $180^\circ$ , then the tuning curve was called centered. We found 30 grid fields with significantly tuned and centered tuning curves.

### **Modeling different prospective or retrospective scenarios**

The following scenarios were applied at the level of individual grid cells.

#### *Movement direction (MD)*

We shifted every trajectory point backwards (negative shift) or forwards (positive shift) along the animal's momentary movement direction (MD). The MD was computed as the orientation of the average of the vectors defined by the previous and the following trajectory segments (the vector pointing from  $(px_{i-1}, py_{i-1})$  to  $(px_i, py_i)$  and the vector pointing from  $(px_i, py_i)$  to  $(px_{i+1}, py_{i+1})$ ), where  $i$  denotes the  $i$ 'th location in the raw position data set. Using the original spike times we recomputed the MD-shifted spike positions by interpolation on the MD-shifted trajectory (Fig. 2A first panel). The explored shifts ranged from -6 to +6 cm in steps of 0.2 cm.

#### *Head direction (HD)*

We shifted every trajectory point along the animal's head direction (HD), given by the vector pointing from the neck LED to the midpoint between the two LEDs at the ears. Using the original spike times we recomputed the HD-shifted spike positions on the HD-shifted trajectory (Fig. 2A second panel). The range of explored shifts was from -6 to +6 cm with steps of 0.2 cm.

## *TIME*

In the scenario "TIME" we decreased (past, -) or increased (future, +) the spike times and recomputed spike positions on the recorded trajectory (Fig. 2A third panel). The range of tested shifts was from -600 to 600 ms with 20 ms steps.

## *Distance along trajectory (DAT)*

In the DAT scenario we moved spikes by a fixed distance either backwards (-) or forwards (+) along the trajectory. From these new positions on the recorded trajectory we recomputed new spike times (Fig. 2A fourth panel). The TIME and the DAT scenarios are related to each other by the animal's speed. The range of tried shifts was from -6 to 6 cm with 0.2 cm steps.

## **Optimization in different dimensions**

At every shift we reran the original field detection algorithm. If there was a field detected and if the grid field center was in the 5 cm vicinity of the field center detected at 0 shift, we kept the grid field center and labeled spikes to it as described in 'Grid field detection'. We computed a MI for the field at every shift parameter when there was a detectable field. We chose the optimal shift where MI was closest to 0 (most uniform inbound-outbound tuning).

## **Speed division**

We divided every cells' spiking data into 4 equal sized quartiles based on the momentary running speed when spikes were fired. We rerun the field detection algorithm on the 4 quartiles separately and if there was a field center detected in the 5 cm vicinity of a field center of the undivided spiking data we computed the modulation index and the optimal shifts.

## **Field size**

Field size was computed as:

$$Fieldsize = \sqrt{\frac{\sum D_i^2}{n}}$$

where  $n$  is the number of spikes labeled as members of the grid field and  $D_i$  is the spatial distance of the  $i$ 'th spike position in the field from the grid-field center. All field sizes computed for a grid field during optimization were normalized by the field size computed at 0 shift (FS).

### **Experimental design and statistical analysis**

We analyzed data recorded by Latuske et al. (2015) and refer the reader to this publication for details on the experimental design. All our analyses were performed in Python 2.7.6. Specific statistical tests used are stated throughout the text. The T-test is taken from `scipy.stats`. Spearman and Pearson correlations were tested for significance by independently shuffling the two coordinates of the respective data points and computing the corresponding correlation for each new sample. The p-value for correlation is given by the fraction of samples for which the correlation value was larger than in the original sample.

## *Results*

### **Grid-cell data can show non-uniform inbound-outbound tuning**

If grid cells encoded the animal's current allocentric position, a cell's firing should not depend on whether the animal is running into one of its firing fields, out of the field, or in some other direction relative to the firing-field center. This should even be true for conjunctive cells, which encode location together with the head's absolute direction in space (Sargolini et al., 2006). On the other hand, deviations from a flat tuning curve in coordinates relative to the grid-field center would indicate that grid cells do not encode the animal's current position but one shifted in time or space. A similar effect was reported by Huxter et al. (2008), who showed for hippocampal place cells from dorsal CA1 that shifting spike positions along the animal's current movement direction by about three centimeters leads to the strongest decrease in the firing-field size. In the present study, we wanted to find out whether the shifts needed to obtain flat tuning curves indicate spatial or temporal transformations or even more complicated representations of the animal location.

In the first step, we studied the angular distribution between the animal's momentary velocity vector and the vector pointing from the spike position to the center of the grid field under study, which we will call the "inbound-outbound angle" (Fig. 1A). Unlike head-direction angles, the inbound-outbound angle represents the orientation of the animal relative to the field center (Fig. 1D) instead of the absolute orientation (Fig. 1C). From these angles we computed an "inbound-outbound firing probability" curve for every grid field, and fitted the data with a cosine model (see Materials and Methods), as shown in Fig. 1E. Based on the modulation amplitude of the cosine fit, we computed modulation indices (MIs) - which measure the modulation amplitude - and peak phases, as described in Materials and Methods. If a grid field's MI was positive and the peak phase was between  $-90^\circ$  and  $90^\circ$ , the field was called "inbound tuned", and "outbound tuned" otherwise (Fig. 1B).

We detected 42 out of 55 significantly tuned grid fields (see Materials and Methods). 40 grid fields had positive MIs and two fields had negative MIs. Most importantly, the mean of the MI distribution ( $0.46 \pm 0.27$ ) was highly significantly different from zero (T-test,  $p = 1.08 \times 10^{-13}$ ) as shown in Fig. 1F; the circular mean of the peak phase distribution was  $-8.55^\circ \pm 4.65^\circ$ , see Fig. 1G. As more than 75% of the grid fields were significantly tuned and more than 95% of the significant fields had a positive MI, there was a clear asymmetry between inbound and outbound firing rates in that grid cells tended to be more active when the animal moved towards the firing field than when it moved away from it.

This phenomenon agrees with the concept of prospective firing (see, e.g., De Almeida et al., 2012).



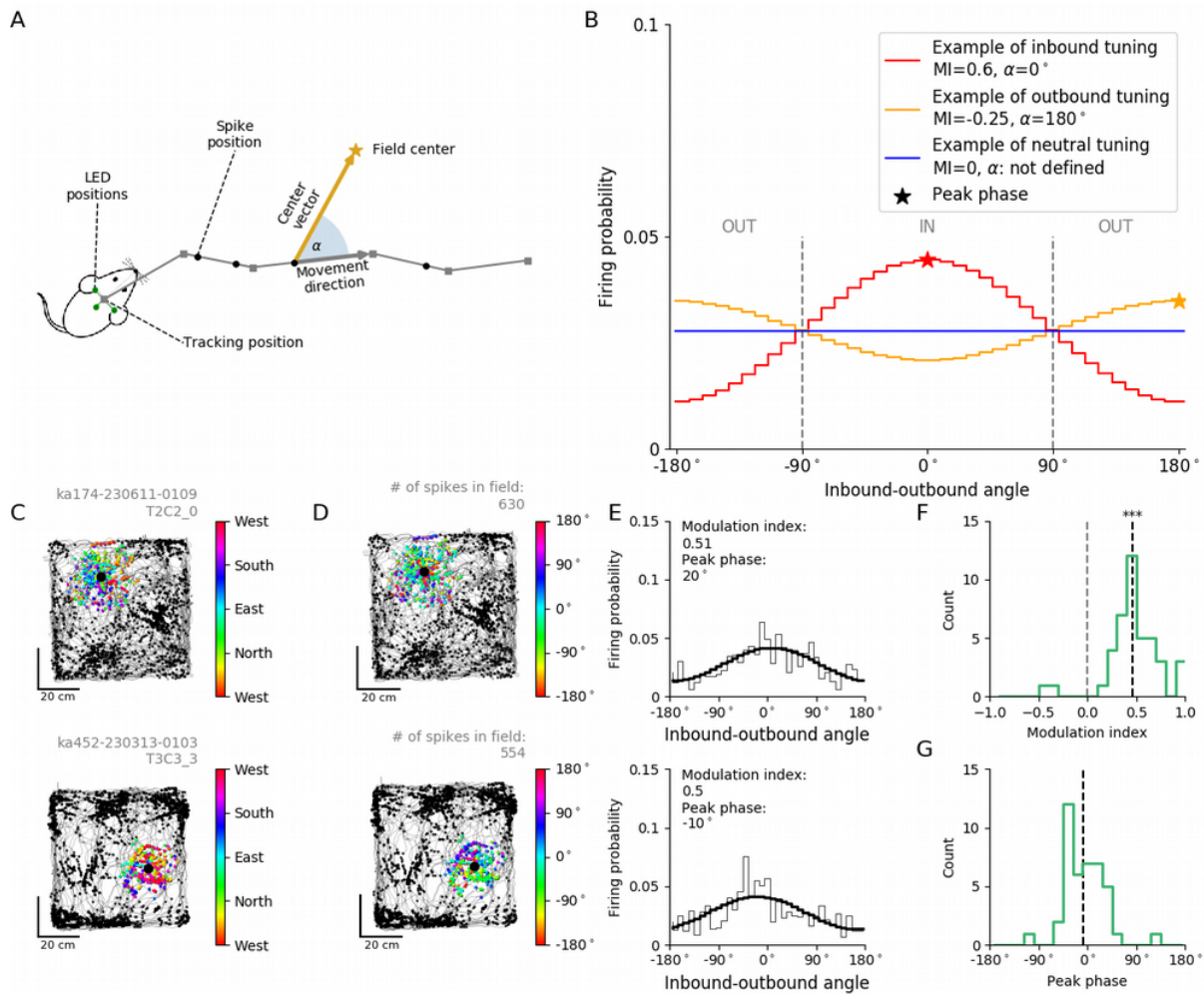


**Figure 1** - Inbound-tuned firing pattern of mouse grid cells

A, Computation of the inbound-outbound angle  $\alpha$ . There were three LEDs (green dots) placed on the head of the animal, from which the tracking position (grey squares) was computed at every sampling point. The positions of the spikes generated by a cell (black dots) were calculated from its spike times by interpolation along the animal trajectory. For all spikes of a particular grid field, inbound-outbound angles were computed as the angles between the momentary movement direction and the vector pointing from the spike position to the center of that grid field.

B, To characterize the inbound-outbound tuning curves, modulation indices (MIs) and peak phases were calculated. For illustrative purposes, three qualitatively different fits are shown, inbound tuned (red), outbound tuned (orange) and a neutral case. The MIs show the tuning strength and their signs tell whether the tuning is inbound (+) or outbound (-). Asterisks denote the fits' peak phase.

C, Absolute running directions of an animal when spikes were fired for two example grid fields. (Grey: trajectory, black: spikes that are not members of the grid field, large black dot: center of the grid field, colored dots: spikes that are members of the firing field, colored by the absolute running direction).

D, Inbound-outbound, egocentric running direction of an animal when spikes were fired. Same two example grid fields as in C (Spikes belonging to the particular grid field are colored by the running direction relative to the grid field center (inbound-outbound angle)).

E, Inbound-outbound firing probabilities for the two example grid fields, together with their cosine fits. (Thin black line: binned firing probability, thick black line: cosine fit, black text: MI and peak phase of the cosine fit).

F, Relative frequency of modulation indices of the significantly tuned grid fields. (Grey dashed line: expected mean of the modulation indices, i.e. zero, black dashed line: Mean of the modulation indices. 3 asterisks note that the mean of the distribution of MI-s is significantly different from 0, T-test,  $p < 0.01$ ).

G, Relative frequency of peak phases of the significantly tuned grid fields. (Black dashed line: Circular mean of the peak phases).

## **Inbound firing rate tuning vanishes when shifting spikes ahead both in space and in time**

To explain these observations, we tested four alternative hypotheses:

**MD** ("movement direction"): grid cells anticipate future locations along the momentary velocity vector;

**HD** ("head direction"): the diodes used to track the animal's location do not represent the position along the head-axis which the grid cells actually encode;

**TIME**: grid cells anticipate future locations using a fixed temporal interval;

**DAT** ("distance along trajectory"): grid cells anticipate future locations along the trajectory with a fixed spatial distance from the current location.

Hypotheses MD and HD assume that a spike is fired in the correct moment, but not for the position where it was recorded. To test whether this could explain the data, we shifted the trajectory points in space and remapped the spikes onto the shifted trajectory (Fig. 2A, first and second subpanel). By altering the size of the shift, we investigated whether approximately flat tuning curves could be obtained. The optimal shifts obtained in that manner might reveal the type of anticipation used and/or the mismatch between the tracing position and the animal's own sense of self-location.

Similarly, the TIME scenario assumes that a spike was fired earlier or later in time, i.e., prospectively or retrospectively, so we decreased or increased the spike time (Fig. 2A, third subpanel). Finally, the DAT shift assumes that grid cells anticipate along their curved movement trajectory, so we shifted their spikes by a fixed distance along the trajectory (arc length) and recomputed the new spike times (Fig. 2A, fourth subpanel). The TIME and DAT shifts are related by the momentary speed.

Every cell's data were shifted according to the four different scenarios (three when there was no head direction data provided in the recorded data). We shifted both backwards (negative shifts) and forwards (positive shifts). For each shift parameter all the data of one cell were shifted by that given parameter (i.e., if the time shift was -400 ms, all spike times of the cell were decreased by -400 ms).

We only studied optimization curves of grid fields which were significantly inbound-outbound tuned and had a centered peak phase (peak phase less than  $\pm 45^\circ$  away from  $0^\circ$  or  $180^\circ$ ) for zero shift (see also Materials and Methods). We optimized for flat inbound-outbound tuning curves. All four scenarios showed inverted sigmoidal MI optimization curves (Fig. 2B). The optimal shift for a grid field was defined as that shift for which MI was closest to zero, i.e., the cosine fit to the tuning curve at that shift was as flat as possible. Every shifting paradigm resulted mainly in positive optimal shifts, significantly different from zero shift as shown in Fig. 2C (T-test with Bonferroni correction, MD:  $3.17 \pm 1.65$  cm,  $p = 3.12 \times 10^{-11}$ ; HD:  $2.72 \pm 1.49$  cm,  $p = 8.40 \times 10^{-8}$ ; TIME:  $0.17 \pm 0.09$  s,  $p = 4.03 \times 10^{-11}$ ; DAT:  $1.97 \pm 1.95$  cm,  $p = 7.78 \times 10^{-6}$ ). As illustrated in Fig. 2D, the means of the modulation indices at optimal shifts of all four scenarios were not significantly different from zero (T-test with Bonferroni correction, MD:  $-0.020 \pm 0.141$ ,  $p = 0.46$ ; HD:  $0.056 \pm 0.153$ ,  $p = 0.11$ ; TIME:  $-0.001 \pm 0.165$ ,  $p = 0.96$ ; DAT:  $0.006 \pm 0.150$ ,  $p = 0.82$ ). We conclude that the optimization indeed flattened the tuning curves such that on average, they are no longer inbound or outbound tuned.

One might expect that the higher modulation index MI is, the higher the expected optimal shift. In other words, when the field is more inbound tuned, flattening it is likely to require a larger forward shift. To test this hypothesis, we calculated the Spearman correlations between the MIs before shifting and the optimal shifts and found that this was indeed true for the MD ( $r_s = 0.71$ ,  $p = 1.27 \times 10^{-5}$ ), TIME ( $r_s = 0.61$ ,  $p = 3.46 \times 10^{-4}$ ) and DAT ( $r_s = 0.74$ ,  $p = 3.10 \times 10^{-6}$ ) shifts as shown in Fig. 2E. For HD we obtained a positive but non-significant correlation ( $r_s = 0.38$ ,  $p = 0.08$ ). Without the outlier at  $MI = 0.95$ , the regression line ( $m = 4.7$  cm,  $b = 1.06$  cm,  $r_s = 0.60$ ) would resemble those for the MD and DAT optimizations.

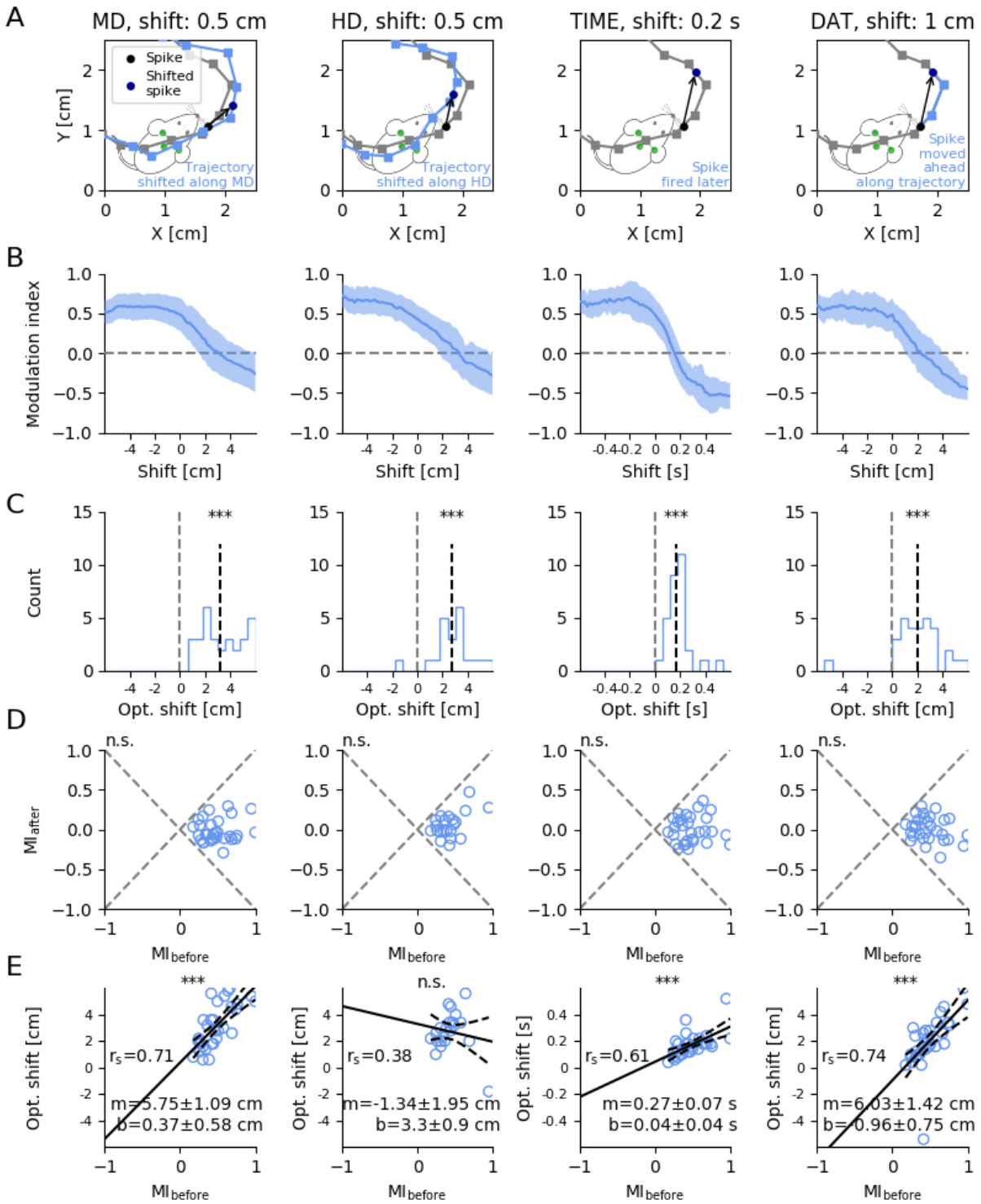


**Figure 2** - Alternative scenarios to flatten inbound-tuned firing rates

A, Visualization of the four different scenarios that were used for optimization. For MD and HD we shifted the trajectory points forwards and backwards along the movement direction or head

direction and kept the spike times. For TIME we assumed that spikes were fired with a positive or negative temporal offset, so we shifted the spike times and remapped them on the original trajectory. For DAT we moved spikes by a given distance along the trajectory and recomputed the spike times from the new spike positions.

B, Mean optimization curves in the different scenarios of the significant and centered fields. MI is shown as a function of the tested shift (Blue line: mean MI at shift, shaded area: SD around the mean, Grey dashed line: optimal modulation index).

C, Distributions of optimal shifts in the different optimization scenarios. (Black dashed line: Mean of optimal shifts; three asterisks indicate that the mean of the distribution is highly significantly different from zero, T-test  $p < 0.01/4$ )

D, Modulation indices before and after optimization in the different optimization scenarios. The modulation indices are decreased after optimization and their means were never significantly different from zero (n.s.: not significant, T-test,  $p > 0.05/4$ ) (Grey dashed lines: lines of constant performance in terms of absolute MI values.)

E, Optimal shifts as a function of MIs before shifting. The fit of regression lines were highly significant for the reliability of fit for MD, TIME and DAT. Black solid line: regression line, black dashed line: 95% confidence interval,  $r_s$ : Spearman correlation value,  $m$ : slope of the regression line,  $b$ : intercept of the regression line, SD: standard error of the estimate. Three asterisks indicate that the Spearman correlation is highly significant ( $p < 0.01/4$ ) and n.s. notes not significant ( $p > 0.05/4$ ).

## Speed-dependency of anticipation

A purely spatial anticipation or a mismatch between the animal's perceived localization and that measured by the experimenter should not depend on the animal's speed. However, MI increases, although non-significantly with the mean running speed in the field ( $r_s=0.29$ ,  $p=0.069$ ), suggesting that there could be a temporal aspect in anticipation (Fig. 3A). A closer look at how the optimal shift depends on the animal's speed shows that the optimal shift for TIME does only change slightly with changing speed (third panel, Fig. 3B). For a rough comparison of the speed dependency in the time-shift paradigm versus those in the other shift-scenarios, the physical dimensions of the slopes, i.e.,  $s^2/cm$  versus  $s$ , need to be related by a characteristic animal speed, which we take to be 10-15 cm/s (the average of mean movement speed in grid fields is  $13.91\pm 4.00$  cm/s). With this setting, the slope of the regression line of the TIME scenario ( $m=0.005$   $s^2/cm$ ) translates into an effective slope of  $m=0.04-0.06$  s, which is of the same order of magnitude as the MD (0.21 s), HD (0.13 s) and DAT (0.24 s) slopes, but only about a third as large. These rough estimates suggest that the optimal shifts vary less in the TIME scenario than in the other three shift paradigms, with an average temporal anticipation of around 170 ms.

To investigate whether the speed dependency of the anticipation is true in sessions, we divided every cells' spiking data into 4 quartiles based on the momentary running speed. We found that indeed, the ranks of the speed quartiles were highly significantly correlated with the corresponding modulation indices ( $r_s=0.39$ ,  $p=6.20\cdot 10^{-6}$ ) (Fig. 3C). Furthermore, when we correlated the optimal shifts of the quartiles in the case of one spatial scenario, namely MD, we found a highly significant correlation ( $r_s=0.49$ ,  $p=5.19\cdot 10^{-8}$ ) (Fig 3D). On the other hand, the TIME optimal shifts showed a close to zero, non-significant correlation with the quartiles' ranks ( $r_s=0.09$ ,  $p=0.34$ ) (Fig. 3D). This suggests that in-session the strength of inbound tuning is speed dependent. This could be explained by a consistent temporal anticipation and thus speed dependent spatial optimal shifts along the trajectory of the animal. More detailed analysis on the level of individual runs through grid fields

could not be unambiguously performed, because the spike counts per run would not provide enough spikes for reliably detecting the grid field centers at the tested shift parameters.



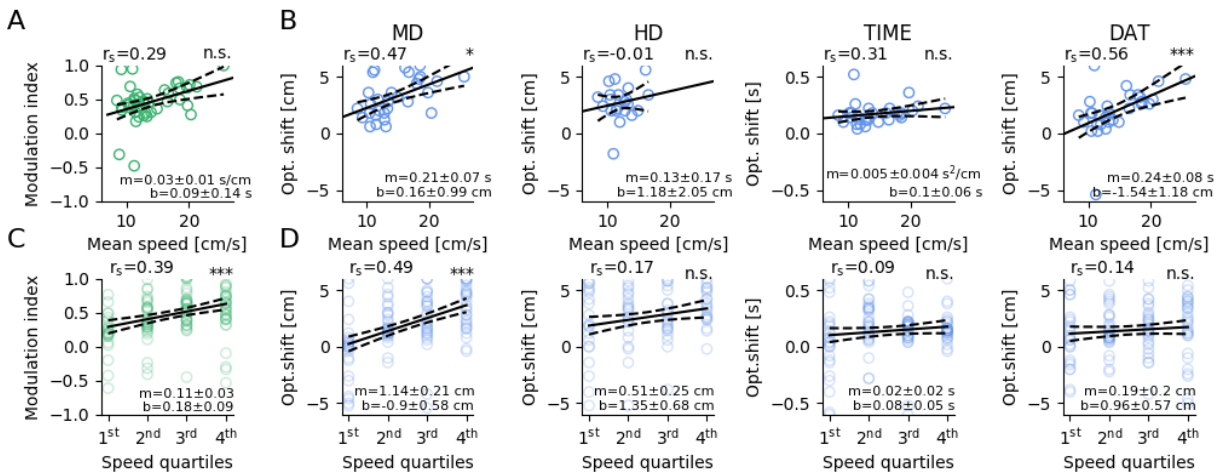


**Figure 3** – Effect of speed on modulation index and optimal shift

A, Modulation indices before optimization as a function of mean running speed within the grid fields.

B, Optimal shifts as a function of within-grid-field mean running speed before optimization for the four optimization scenarios.

C, Modulation indices of the quartiles before optimization as a function of the quartiles' rank.

D, Optimal shifts of the quartiles as a function of the quartiles' rank for the four different optimization scenarios.

Black solid lines: regression lines, black dashed lines: 95% confidence intervals,  $r_s$ : Spearman correlation values,  $m$ : slopes of the regression lines,  $b$ : intercepts of the regression lines, single asterisks: significance value for correlation (B:  $p < 0.05/4$ ), three asterisks: significance value for correlation (C:  $p < 0.01$ , D:  $p < 0.01/4$ ), n.s.: significance value for correlation (A:  $p > 0.05$ , B,D:  $p > 0.05/4$ ) (correction for multiple testing).

## Optimization of firing-field size

Other authors, such as Huxter et al. (2008) and Kropff et al. (2015), have tested grid and place cell coding by shifting spikes ahead either in space or time so as to obtain the smallest grid or place-cell field sizes (FS). We repeated this analysis for the four shifting scenarios (Fig. 4A). Optimal shifts were mostly positive for the smallest field size and the MD, TIME and the DAT optimal shifts were significantly different from zero (T-test with Bonferroni correction, MD:  $1.85 \pm 2.54$ cm,  $p=4.79 \times 10^{-4}$ , HD:  $1.65 \pm 0.86$ cm,  $p=0.018$ , DAT:  $1.99 \pm 2.43$  cm,  $p=1.27 \times 10^{-4}$ , TIME:  $0.115 \pm 0.226$ s,  $p=0.013$ ), as shown in Fig. 4B,C. These shifts are somewhat smaller than those from the inbound-outbound tuning optimization, but the difference is significant only for MD (T-test, MD:  $p=0.022$ , HD:  $p=0.143$ , TIME:  $0.228$ , DAT:  $p=0.973$ ). On average, the field sizes decreased to values between 90 and 95% of their starting values (MD:  $0.95 \pm 0.06$ , HD:  $0.91 \pm 0.06$  TIME:  $0.91 \pm 0.08$ , DAT:  $0.92 \pm 0.06$ ). These results demonstrate that, similar to our results for inbound-outbound tuning curves, firing-field sizes can be optimized in different ways without a particular preferred shift dimension. In other words, being able to reduce the firing-field size along a certain dimension does not imply that this dimension is in any way unique.

We then asked how strongly the optimization for MI or FS differed. When we optimized for the modulation index to be close to zero, all four optimization scenarios showed decreased average field sizes that were highly significant for HD and TIME (T-test with Bonferroni correction, MD:  $0.98 \pm 0.06$   $p=0.037$ , HD:  $0.95 \pm 0.05$   $p=1.12 \times 10^{-4}$ , TIME:  $0.97 \pm 0.03$   $p=1.64 \times 10^{-6}$ , DAT:  $0.97 \pm 0.06$   $p=0.031$ ), see Fig. 4D. When we minimized the FS (Fig. 4E), on the other hand, the average modulation indices, which initially had an average of 0.48 for MD, TIME and DAT, and 0.42 for HD, decreased strongly (T-test, MD:  $0.36 \pm 0.30$ ,  $p=4.89 \times 10^{-7}$ , HD:  $0.25 \pm 0.26$ ,  $p=3.29 \times 10^{-4}$ , TIME:  $0.51 \pm 0.47$ ,  $p=2.45 \times 10^{-6}$ , DAT:  $0.48 \pm 0.34$ ,  $p=2.69 \times 10^{-8}$ ) towards near-zero values (MD: 0.12, HD: 0.18, TIME: -0.02, DAT: 0.01). This finding shows that, indeed, optimizing for FS goes hand in hand with achieving small modulations in the inbound-outbound tuning curves. Thus,

although the two optimization schemes involve fundamentally different measures, they nevertheless result in rather similar final configurations.

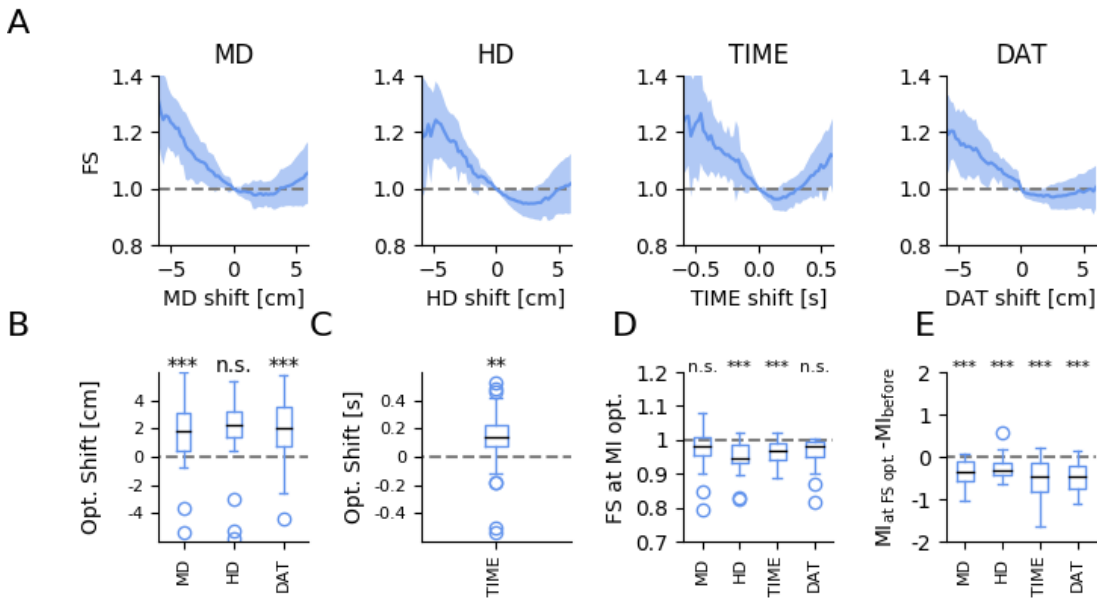


**Figure 4** – Optimizing firing fields

A, Mean optimization curves for the relative field size (FS) in the different scenarios. FS is shown as a function of the tested shift (Blue line: mean MI at shift, shaded area: SD around the mean, Grey dashed line: relative FS at zero shift, i.e., unity).

B, Distributions of spatial shifts when optimizing for FS (n.s.: not significant, T-test,  $p > 0.05/3$ , three asterisks: T-test,  $p < 0.01/3$ ).

C, Distribution of optimal TIME shifts for the smallest FS (two asterisks: T-test,  $p < 0.02$ ).

D, FS distribution when optimizing for the modulation indices to be close to zero (n.s.: not significant, T-test,  $p > 0.05/4$ , three asterisks: T-test,  $p < 0.01/4$ ).

E, Distribution of the differences between initial MI and optimized values when small field sizes are the target of optimization. (three asterisks: T-test,  $p < 0.01/4$ )

## Combined optimization along the HD and TIME dimensions

Although a constant temporal shift is consistent with a speed-dependent spatial shift we cannot rule out that both the displacement of the LEDs relative to animal's perceived location and temporal anticipation lead to the high modulation indices of inbound-outbound tunings. Therefore, we ran a combined tuning-curve optimization where we varied both along the HD and TIME-dimension and picked the optimal combination of spatial and temporal shifts (parameter ranges: TIME: -0.1 s to +2.0 s in 0.02 s steps, HD: -1 cm to +5 cm in 0.2 cm steps). The two-dimensional optimizations resulted in a continuum of optimal shifts (Fig. 5A). This continuum resembles a straight line, in agreement with a linear relation between the HD and TIME components of the joint shift ( $r=-0.998$ ,  $p=8*10^{-52}$ ). The slope of the linear fit to the average optimization plane ( $-21.74 \pm 0.23$  cm/s) is of the same order though somewhat larger than the typical running speed of the studied mice (population-averaged median speed in grid fields:  $13.47 \pm 4.44$  cm/s) which might suggest that the trade-off between a spatial shift and temporal anticipation is related to the animals' movement characteristics. The continuum of optimal solutions underscores the difficulty in assigning a unique cause to the inbound-outbound tuning of grid cells.

When one simultaneously minimizes the firing-field size along the HD and TIME dimensions, a shallow minimum appears at the population level (Fig. 5B). From a parabolic fit of the data for  $FS < 1$ , optimal spatial shifts were calculated as 2.31 cm, optimal temporal shifts were 0.036 s. The two-dimensional HD-TIME optimization does not lead to significantly better improvements in FS compared to the one-dimensional HD or TIME optimizations ( $p=0.87$  and  $p=0.85$ , respectively). The ellipsoidal near-optimal field-size contours in Fig. 5B are tilted and again suggest a trade-off between temporal anticipation and spatial offset, in qualitative agreement with the tuning-curve results.

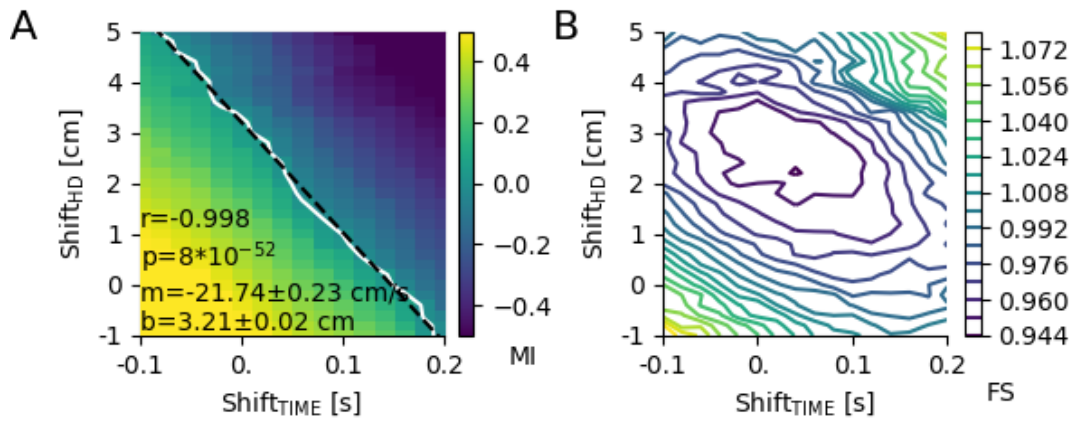


**Figure 5** – Population average of combined HD and TIME optimizations

A, When spikes are simultaneously shifted along the HD and TIME dimension, a continuum of optimal solutions with vanishing MI emerges, here shown for the average across all analyzed grid fields. This continuum illustrates the trade-off between spatial mismatch (LED position vs. perceived location) and temporal anticipation.

White line: zero-crossing of the mean optimization plane, black dashed line: regression line,  $r_s$ : Pearson correlation value,  $p$ : p-value for Pearson correlation,  $m$ : slope of the regression line,  $b$ : intercept of the regression line

B, When joint shifts along the HD and TIME dimension are used to minimize firing-field size, a shallow minimum can be observed (HD shift:  $2.79 \pm 1.72$  cm, TIME shift:  $0.024 \pm 0.070$  s).

## *Discussion*

Analyzing the dataset of Latuske et al. (2015) we found that grid cells in mice fire prospectively (positive MI) almost exclusively. This result differs from findings by De Almeida et al. (2012) who reported that rat grid cells can also be in a retrospective mode. Furthermore, the spatial anticipation measured by De Almeida et al. was up to 15 cm, whereas pure spatial shifts calculated in this paper are around 3 cm. The differences might partly reflect differences in animal size as well as differences in the experimental design – fast straight runs on linear tracks without foraging in the study of De Almeida et al. versus curved trajectories during foraging in an open arena in the study of Latuske et al. – that result in different behavioral states.

To better understand the inbound-outbound firing characteristics in the dataset of Latuske et al. we studied four different scenarios – anticipation along the movement direction (MD), head direction (HD), TIME and DAT (distance along trajectory). The optimal spatial shifts measured in the MD, HD, and DAT paradigm were around 3 cm. Shifts in that range were also reported by Huxter et al. (2008) who recorded place cells in rat hippocampus (CA1) and minimized the place-field size along the movement direction. These authors then assumed that the apparent prospective firing results from a mismatch between the LED position and the animal's perceived location. However, minimizing firing-field sizes can again be done along the same dimensions as minimizing tuning-curve modulations (Fig. 4). For all four dimensions investigated, shifting spikes can reduce the firing-field size – as for tuning-curves, there is no special role for shifts along the movement direction. This finding implies that the place-cell data of Huxter et al. (2008) might possibly also have an interpretation as true temporal anticipation or some mixture of spatial and temporal components, as in our work. The temporal anticipation scenario was also supported by our finding that in-session the modulation indices and the MD spatial optimal shifts are speed dependent. This could be explained by the consistent TIME optimal shifts which were shown to be speed independent (Fig. 3).

For rat CA1 place-cell ensemble coding a theta-sequence look-ahead with a goal-dependent extent was reported by Wilkenheiser and Redish (2015). Since in the experimental data analyzed in our study there were no goals present the results cannot be directly compared. However, the prospective fashion of the coding is supported by those findings. For grid cells in the superficial layers of medial entorhinal cortex of rats, indications of a similar look-ahead have been found as well (O'Neill et al. 2017). In addition, recent evidence suggests that hippocampal theta sequences extend to MEC and represent forward-directed sweeps as well as left-right alternations of prospective trajectories in egocentric coordinates (Gardner et al., 2019). The detailed relation between these phenomena and the modulated inbound-outbound tuning curves studied here has not been addressed yet.

The optimal TIME shift found in the present study is around 170 ms, which clearly differs from the 70 ms reported by Kropff et al. (2015) for rat grid cells with theta-modulated speed cell input (T-test,  $p=1.29 \times 10^{-6}$ ). In both studies, however, the spatial anticipation along the trajectory showed the same qualitative running-speed dependency. Further analysis is needed to reconcile the quantitative differences. On the other hand, when we optimized for minimal field size, as in Kropff et al. (2015), the distribution of temporal shifts was not significantly different from 70 ms (T-test,  $p=0.31$ ). In other words, optimizing for small field size results in smaller optimal shifts than when focusing on inbound-outbound tuning.

The present exploratory study underscores the importance of distinguishing between spatial aspects and temporal anticipation and points to a trade-off once both types of shifted activity are jointly considered for optimizing the inbound-outbound tuning curves. Given the optimization criteria (i.e. the modulation index) should be the closest to zero and not reaching a local extremum, the two dimensional inverted sigmoidal optimization plane has many zero crossings. This trade-off could be especially relevant when the animal is taking straight runs through a grid field. In these cases the temporal and the spatial forward shifts would be both along the same directions. In such scenarios, the spatial and temporal anticipation are hard to distinguish. Furthermore, the trade-off would be

more obvious if the running speed of the animal during these runs is relatively constant. In addition, comparison with the published literature shows that there remain a number of open issues. We do hope that our investigation will trigger follow-up studies to clarify these questions.



## *References*

- Blair HT, Sharp PE. 1995. Anticipatory head direction signals in anterior thalamus: evidence for a thalamocortical circuit that integrates angular head motion to compute head direction. *Journal of Neuroscience*, 15(9):6260–6270.
- Comaniciu D, Meer P. 2002. Mean Shift: A robust approach toward feature space analysis. *IEEE Transactions on Pattern Analysis and Machine Intelligence*, pp. 603-619
- De Almeida L, Idiart M, Villavicencio A, Lisman J. 2012. Alternating predictive and short-term memory modes of entorhinal grid cells. *Hippocampus*, 22(8):1647–1651.
- Gardner, RJ, Vollan AZ, Moser M-B, Moser EI 2019. A novel directional signal expressed during theta sequences. *Society for Neuroscience Meeting 604.13/AA9*
- Hafting T, Fyhn M, Molden S, Moser MB, and Moser EI. 2005. Microstructure of a spatial map in the entorhinal cortex. *Nature*, 436(7052):801–806.
- Huxter JR, Senior TJ, Allen K, Csicsvari J. 2008. Theta phase-specific codes for two-dimensional position, trajectory and heading in the hippocampus. *Nature Neuroscience*, 11(5):587–594.
- Kropff E, Carmichael JE, Moser MB, Moser EI. 2015. Speed cells in the medial entorhinal cortex. *Nature*, 523(7561):419–424.
- Lever C, Burton S, Jeevjee A, O’Keefe J, Burgess N. 2009. Boundary vector cells in the subiculum of the hippocampal formation. *The Journal of neuroscience: the official journal of the Society for Neuroscience*, 29(31):9771–9777.
- Muller RU, Kubie JL. 1989. The firing of hippocampal place cells predicts the future position of freely moving rats. *Journal of Neuroscience*, 9(12):4101–4110.
- O’Keefe J, Dostrovsky J. 1971. The hippocampus as a spatial map. preliminary evidence from unit activity in the freely-moving rat. *Brain Research*, 34(1):171 – 175.

O'Neill J, Boccara CN, Stelle F, Schoenenberger P, Csicsvari J. 2017. Superficial layers of the medial entorhinal cortex replay independently of the hippocampus. *Science* 355: 184-188.

Sargolini F, Fyhn M, Hafting T, McNaughton BL, Witter MP, Moser MB, Moser EI. 2006. Conjunctive representation of position, direction, and velocity in entorhinal cortex. *Science*, 312(5774): 758–762.

Sharp PE. 1999. Comparison of the timing of hippocampal and subicular spatial signals: Implications for path integration. *Hippocampus*, 9(2):158–172.

Stackman RW, Taube JS. 1998. Firing properties of rat lateral mammillary single units: Head direction, head pitch, and angular head velocity. *Journal of Neuroscience*, 18(21):9020–9037.

Taube JS, Muller RU, Ranck JB. 1990. Head-direction cells recorded from the postsubiculum in freely moving rats. ii. effects of environmental manipulations. *Journal of Neuroscience*, 10(2):436–447.

Wilkenheiser AM, Redish AD. 2015 Decoding the cognitive map: ensemble hippocampal sequences and decision making. *Curr Opin Neurobiology*, 32:8-15.



## 5 Discussion

The two main findings of this thesis can be summarized as follows: First, the *in vivo* burst firing of principal neurons in the medial entorhinal cortex is strongly influenced by the cell-intrinsic voltage response directly following an action potential. Second, grid cells anticipate the animal's future movement. The direct implications of these findings are explained in detail in the discussion sections of the two manuscripts that form the core of this thesis. Here, I will rather highlight some aspects of my findings in the broader context of spatial navigation.

Let me first clarify the relation between anticipation, preplay and replay. In replay, neural representations of previously visited locations are reactivated both in the hippocampus and the entorhinal cortex, typically in a highly time-compressed manner (Wilson & McNaughton, 1994; Foster & Wilson, 2006; Olafsdottir *et al.*, 2016). This has been implicated in the consolidation of spatial memories, see Foster (2017) for a comprehensive review. In preplay, sequential activations of place cells occur that mimic future activity sequences to a goal, even before the animal visits a new or modified enclosure, see, for example Olafsdottir *et al.* (2015). One mechanism for such activations are prewired chains of neurons, to which external stimulus sequences are associated during spatial behavior, as discussed in the paper of Leibold (2020). Finally, anticipation implies a temporal or spatial shift of neural activity.

All three phenomena may aid future behavior but they occur in rather different situations replay and preplay are observed while the animal is resting whereas anticipation is an integral part of neural activity while the animal is moving in its environment. Furthermore, replay and preplay can be temporally distant from the experience of the past or future trajectory segment, whereas anticipation is in the spatial (few cm) or temporal (few 100 ms) vicinity of the navigational experience. It remains an open question whether preplay and replay utilize the shifted reference frames of anticipatory activity.

When learning the locations of goals in a navigational task, the amount of grid cell anticipation could dynamically vary. It was shown that in such an experimental paradigm grid fields move towards the goal location (Boccarda *et al.*, 2019). During this learning process, it is possible that the amount of temporal or spatial anticipation is dynamically decreasing over time, thus showing a drift of the location of the grid field towards the goal.

We have shown that the inbound-outbound tuning in grid fields was dependent on the running speed of the animal. This was also true for some of the optimal spatial shifts. Such a correlation could be explained by a consistent temporal anticipation resulting in higher spatial optimal shifts ahead along the trajectory as the animal runs faster. Thus, assuming that grid cells anticipate in time, I will consider the relationship to theta oscillation and theta sequences.

The interpretation of inbound tuned grid fields is that the firing rate in a grid field is higher when entering the grid field, compared to when leaving it. As this is a sign of anticipation, the firing rate is

higher for future positions than for positions already left behind. In other words, in the case of temporal anticipation this means that the firing rate is higher on the predictive phase of the theta cycle than on the retrospective phase. This is in agreement with Kropff *et al.* (2015) who had shown that the maximal firing rate in the entorhinal cortex is on the predictive phase (look ahead stage) of the theta oscillation. Also, these authors reported that only grid cells whose activity is theta-modulated exhibit anticipatory spiking behavior. Such asymmetric representations in theta sequences for future and past in one cycle were also shown for place cells by Amemiya & Redish (2018). The idea of theta sequences in grid cells have one benefit compared to theta sequences in place cells, namely that the regularity of the grid cell organization within each module results in a finite set of theta sequences that correspond to each movement direction (Zutshi *et al.*, 2017).

Although in rodents, the necessity of theta activity was emphasized by the fact that spatial coding by grid cells require theta oscillation (Brandon *et al.*, 2011), in other species it might be different. For example, the entorhinal cortex of bats does not express a continuous theta oscillation but rather shows theta-bouts ( $\sim 1$  s) during crawling (Yartsev *et al.*, 2011). Additionally, a clear, but weak theta phase locking of grid cells during theta-bouts has been reported (Yartsev *et al.*, 2011). Thus, temporal anticipation in the frame of theta sequences in the bat MEC does not seem plausible.

One particular strength of the spatial navigation field is the extensive depth of theoretical work alongside experimental data. Currently there are various models describing the emergent dynamics and functions of grid cells. One class of models assumes that grid cells implement velocity-controlled oscillatory (VCO) interference effects that lead to the emergence of a hexagonal activity pattern (Hasselmo *et al.*, 2007; Burgess *et al.*, 2007; Burgess, 2008). Brandon *et al.* (2011) showed that in rodents with reduced theta oscillation grid cells lost their spatial periodicity. Although this supports these type of models, it could not be generalized to other species (Yartsev *et al.*, 2011). An alternative class of models are based on continuous attractor networks (CANs). This type of model assumes that grid cells are arranged on a neural sheet with recurrent connections that support repetitive patterns in the activity bumps that move on the neural sheet due to external velocity input (Fuhs & Touretzky, 2006; McNaughton *et al.*, 2006; Burak & Fiete, 2009; Navratilova *et al.*, 2012). The CAN models are supported by the finding that stellate cells in Layer-II of the entorhinal cortex are interconnected via inhibitory interneurons (Couey *et al.*, 2013). Additionally, the observation that the patterns of spike-time cross correlations of grid cells were preserved during different behavioral states is consistent with CAN model predictions (Trettel *et al.*, 2019; Gardner *et al.*, 2019). A hybrid model of combining the two classes was also proposed, in which the VCOs account for theta modulation and phase precession, updating the location according to the movement, i.e. path integrating, and thus CANs provide stability increasing the spatial information (Bush & Burgess, 2014). Our in-depth analysis of grid-cell dynamics could help to improve these models.

In the first manuscript of this thesis we focused on neural dynamics at short time scales. We found that depolarizing afterpotentials shape the *in vivo* burst activity of MEC principal cells.

It would thus be interesting to test how the characteristics of models based on spatially- and theta-modulated inhomogeneous Poisson processes, as in Bush *et al.* (2015) or Stemmler *et al.* (2015), changes as more detailed membrane-potential dynamics are taken into account (for an earlier attempt in this direction, see Navratilova *et al.* (2012)). To reflect the diversity of the experimentally observed depolarizing afterpotentials and burst behavior, this modeling approach should involve cell-type and layer-specific neural descriptions. Furthermore, the behavioral state should also be considered as a parameter, since propensity to burst in grid cells was shown to increase at fast running speeds (Bant *et al.* , 2020). Even a rather simple network model incorporating the experimentally observed membrane-potential dynamics shows promise to shed new light on the dynamic interactions between high-frequency bursters in MEC Layer-II and sparsely bursting neurons in Layer-III, as well as their functional implications. Considering that stellate cells in Layer-II showed prominent DAPs, in a more detailed CAN model one could model the DAP in the membrane potential dynamics with the appropriate inhibitory interconnectivity (Couey *et al.* , 2013). Perineural networks - the proposed regulators of plasticity (Lensjo *et al.* , 2017b), which encapsulate the soma and stretch along the dendrites were also shown to influence spiking variability in the reelin-expressing stellate cells in the MEC (Lensjo *et al.* , 2017a). As we proposed in the first manuscript, DAPs and bursts could trigger plasticity, and modeling how much the presence of perineural nets influence the membrane potential dynamics could test this hypothesis.

The second manuscript shows that grid cells can exhibit non-uniform inbound-outbound tuning and suggests that they anticipate future movements, but the question remained whether in the biological system, such anticipation is calculated in spatial or temporal coordinates or involves both dimensions. The manuscript suggests that there is no simple answer to this question and demonstrates a trade-off if both types of shifted activity are jointly considered. In continuous attractor models of navigation (see, for example, Burak & Fiete (2009)), the external velocity input is used to update the representation of the current location. It would thus be interesting to see whether one can replicate anticipatory activity in such network models by choosing specific velocity inputs and network-intrinsic connections. Such a theoretical approach could indeed clarify the conceptual challenges in distinguishing between spatial and temporal anticipation. Also, both types of models assume movement direction input provided by head direction cells. Theoretical work of Raudies *et al.* (2015) showed that they both fail to produce the hexagonal grid pattern when using head direction information instead of movement direction. Our work also highlights that optimization in these two different spatial scenarios provides slightly different results. Moreover, only the movement direction optimal shifts resembled the correlation between speed and anticipation. This could mean that movement direction information is already encoded in the firing of grid cells.

In the broader context of network organization of the hippocampal formation, grid cells in the medial entorhinal cortex seem to play a crucial role in providing information about the location of the animal. This information combined with the activity of time cells (i.e. the continuously varying

signal in the lateral entorhinal cortex, providing a code for the temporal progression of events) could answer the "where" and "when" questions for forming episodic memories (Sugar & Moser, 2019). Additionally, Gardner *et al.* (2019) assumed that during sleep, a covert grid signal that drifts could exist. Our results on anticipation also showed that grid cells might not only sign the position of the animal, but also convey more complex information with regard to planning. As an alternative idea for grid cells, the work of Kraus *et al.* (2015) showed that information about location was not sufficient to explain the firing activity of grid cells when running on a treadmill in the absence of external dynamic clues and visual flow. They proposed that grid cells could rather do dead reckoning through computation of path distance from a combination of time traveled and running speed. The addressed anticipation shown for grid cells in this thesis also supports the idea that with planning ahead in the future, grid cell firing considers both time, distance traveled and running speed. The findings in this thesis on the spatio-temporal properties of grid cells further contribute to the theoretical framework of navigation and forming memories.

## References

- Alessi, Camilla, Raspanti, Alessandra, & Magistretti, Jacopo. 2016. Two distinct types of depolarizing afterpotentials are differentially expressed in stellate and pyramidal-like neurons of entorhinal-cortex layer ii. *Hippocampus*, **26**(3), 380–404.
- Amemiya, Seiichiro, & Redish, A David. 2018. Hippocampal theta-gamma coupling reflects state-dependent information processing in decision making. *Cell reports*, **22**(12), 3328–3338.
- Bant, Jason S., Hardcastle, Kiah, Ocko, Samuel A., & Giocomo, Lisa M. 2020. Topography in the bursting dynamics of entorhinal neurons. *Cell reports*, **30**(7), 2349 – 2359.e7.
- Boccaro, Charlotte N., Nardin, Michele, Stella, Federico, O'Neill, Joseph, & Csicsvari, Jozsef. 2019. The entorhinal cognitive map is attracted to goals. *Science*, **363**(6434), 1443–.
- Brandon, Mark P., Bogaard, Andrew R., Libby, Christopher P., Connerney, Michael A., Gupta, Kishan, & Hasselmo, Michael E. 2011. Reduction of theta rhythm dissociates grid cell spatial periodicity from directional tuning. *Science*, **332**(6029), 595–599.
- Burak, Yoram, & Fiete, Ila R. 2009. Accurate path integration in continuous attractor network models of grid cells. *Plos computational biology*, **5**(2), 1–16.
- Burgess, Neil. 2008. Grid cells and theta as oscillatory interference: Theory and predictions. *Hippocampus*, **18**(12), 1157–74.
- Burgess, Neil, Barry, Caswell, & O'Keefe, John. 2007. An oscillatory interference model of grid cell firing. *Hippocampus*, **17**(09), 801–12.
- Bush, Daniel, & Burgess, Neil. 2014. A hybrid oscillatory interference/continuous attractor network model of grid cell firing. *Journal of neuroscience*, **34**(14), 5065–5079.
- Bush, Daniel, Barry, Caswell, Manson, Daniel, & Burgess, Neil. 2015. Using grid cells for navigation. *Neuron*, **87**(08), 507–20.
- Buzsáki, Gyorgy, Anastassiou, Costas, & Koch, Christof. 2012. The origin of extracellular fields and currentseeg, ecog, lfp and spikes. *Nature reviews. neuroscience*, **13**(05), 407–20.
- Chrobak, James, & Buzsáki, Gyorgy. 1998. Gamma oscillations in the entorhinal cortex of the freely behaving rat. *The journal of neuroscience : the official journal of the society for neuroscience*, **18**(02), 388–98.
- Colgin, Laura, Denninger, Tobias, Fyhn, Marianne, Hafting, Torkel, Bonnevie, Tora, Jensen, Ole, Moser, May-Britt, & Moser, Edvard. 2009. Frequency of gamma oscillations routes flow of information in the hippocampus. *Nature*, **462**(11), 353–7.



- Couey, Jonathan J, Witoelar, Aree, Zhang, Sheng-Jia, Zheng, Kang, Ye, Jing, Dunn, Benjamin, Czajkowski, Rafal, Moser, May-Britt, Moser, Edvard I, Roudi, Yasser, & Witter, Menno P. 2013. Recurrent inhibitory circuitry as a mechanism for grid formation. *Nature neuroscience*, **16**(3), 318–324.
- Cressant, Arnaud, Muller, Robert, & Poucet, Bruno. 2002. Remapping of place cell firing patterns after maze rotations. *Experimental brain research. experimentelle hirnforschung. experimentation crbrale*, **143**(05), 470–9.
- de Almeida, Licurgo, Idiart, Marco, Villavicencio, Aline, & Lisman, John. 2012. Alternating predictive and short-term memory modes of entorhinal grid cells. *Hippocampus*, **22**(08), 1647–51.
- Diehl, Geoffrey, Hon, Olivia, Leutgeb, Stefan, & Leutgeb, Jill. 2017. Grid and nongrid cells in medial entorhinal cortex represent spatial location and environmental features with complementary coding schemes. *Neuron*, **94**(03).
- Doeller, Christian F., Barry, Caswell, & Burgess, Neil. 2010. Evidence for grid cells in a human memory network. *Nature*, **463**(7281), 657–661.
- Domnisoru, Cristina, Kinkhabwala, Amina, & Tank, David. 2013. Membrane potential dynamics of grid cells. *Nature*, **495**(02).
- Foster, David. 2017. Replay comes of age. *Annual review of neuroscience*, **40**(07), 581–602.
- Foster, David, & Wilson, Matthew. 2006. Reverse replay of behavioural sequences in hippocampal place cells during the awake state. *Nature*, **440**(04), 680–3.
- Foster, David J., & Wilson, Matthew A. 2007. Hippocampal theta sequences. *Hippocampus*, **17**(11), 1093–1099.
- Fuhs, Mark, & Touretzky, David. 2006. A spin glass model of path integration in rat medial entorhinal cortex. *The journal of neuroscience : the official journal of the society for neuroscience*, **26**(05), 4266–76.
- Fyhn, Marianne, Molden, Sturla, Witter, Menno, Moser, Edvard, & Moser, May-Britt. 2004. Spatial representation in the entorhinal cortex. *Science (new york, n.y.)*, **305**(09), 1258–64.
- Fyhn, Marianne, Hafting, Torkel, Treves, Alessandro, Moser, May-Britt, & Moser, Edvard. 2007. Hippocampal remapping and grid realignment in entorhinal cortex. *Nature*, **446**(04), 190–4.
- Gardner, Richard J., Lu, Li, Wernle, Tanja, Moser, May-Britt, & Moser, Edvard I. 2019. Correlation structure of grid cells is preserved during sleep. *Nature neuroscience*, **22**(4), 598–608.

- Hafting, Torkel, Fyhn, Marianne, Molden, Sturla, Moser, May-Britt, & Moser, Edvard. 2005. Microstructure of a spatial map in the entorhinal cortex. *Nature*, **436**(09), 801–6.
- Hafting, Torkel, Fyhn, Marianne, Bonnevie, Tora, Moser, May-Britt, & Moser, Edvard. 2008. Phase precession in entorhinal grid cells. *Nature*, **453**(07), 1248–52.
- Hasselmo, Michael, Giocomo, Lisa, & Zilli, Eric. 2007. Grid cell firing may arise from interference of theta frequency membrane potential oscillations in single neurons. *Hippocampus*, **17**(12), 1252–71.
- Hayman, Robin, Verriotis, Madeleine A, Jovalekic, Aleksandar, Fenton, Andr A, & Jeffery, Kathryn J. 2011. Anisotropic encoding of three-dimensional space by place cells and grid cells. *Nature neuroscience*, **14**(9), 1182–1188.
- Kraus, Benjamin J, Brandon, Mark P, Robinson, Robert J, 2nd, Connerney, Michael A, Hasselmo, Michael E, & Eichenbaum, Howard. 2015. During running in place, grid cells integrate elapsed time and distance run. *Neuron*, **88**(3), 578–589.
- Kropff, Emilio, Carmichael, James, Moser, May-Britt, & Moser, Edvard. 2015. Speed cells in the medial entorhinal cortex. *Nature*, **523**(07).
- Latuske, Patrick, Toader, Oana, & Allen, Kevin. 2015. Interspike intervals reveal functionally distinct cell populations in the medial entorhinal cortex. *The journal of neuroscience : the official journal of the society for neuroscience*, **35**(08), 10963–76.
- Leibold, Christian. 2020. A model for navigation in unknown environments based on a reservoir of hippocampal sequences. *Neural networks*, **124**(01).
- Lensjo, Kristian Kinden, Christensen, Ane Charlotte, Tennoe, Simen, Fyhn, Marianne, & Hafting, Torkel. 2017a. Differential expression and cell-type specificity of perineuronal nets in hippocampus, medial entorhinal cortex, and visual cortex examined in the rat and mouse. *eneuro*, **4**(3), ENEURO.0379–16.2017–.
- Lensjo, Kristian Kinden, Lepperød, Mikkel Elle, Dick, Gunnar, Hafting, Torkel, & Fyhn, Marianne. 2017b. Removal of perineuronal nets unlocks juvenile plasticity through network mechanisms of decreased inhibition and increased gamma activity. *J. neurosci.*, **37**(5), 1269–.
- Lever, Colin, Burton, Stephen, Jeewajee, Ali, O’Keefe, John, & Burgess, Neil. 2009. Boundary vector cells in the subiculum of the hippocampal formation. *The journal of neuroscience : the official journal of the society for neuroscience*, **29**(09), 9771–7.
- Mathis, Alexander, Herz, Andreas, & Stemmler, Martin. 2012. Optimal population codes for space: Grid cells outperform place cells. *Neural computation*, **24**(05), 2280–317.

- Mcnaughton, Bruce, Battaglia, Francesco, Jensen, Ole, Moser, Edvard, & Moser, May-Britt. 2006. Path integration and the neural basis of the cognitive map.. *Nature reviews. neuroscience*, **7**(09), 663–78.
- Moser, Edvard, Kropff, Emilio, & Moser, May-Britt. 2008. Place cells, grid cells, and the brain’s spatial representation system. *Annual review of neuroscience*, **31**(08), 69–89.
- Muller, Robert, & Kubie, John. 1990. The firing of hippocampal place cells predicts the future position of freely moving rats. *The journal of neuroscience : the official journal of the society for neuroscience*, **9**(01), 4101–10.
- Navratilova, Zaneta, Giocomo, Lisa, Fellous, Jean-Marc, Hasselmo, Michael, & Mcnaughton, Bruce. 2012. Phase precession and variable spatial scaling in a periodic attractor map model of medial entorhinal grid cells with realistic after-spike dynamics. *Hippocampus*, **22**(04), 772–89.
- O’Keefe, J, & Dostrovsky, Jonathan. 1971. The hippocampus as a spatial map. preliminary evidence from unit activity in the freely-moving rat. *Brain research*, **34**(12), 171–175.
- O’Keefe, John, & Recce, Michael. 1993. Phase relationship between hippocampal place units and the eeg theta rhythm. *Hippocampus*, **3**(07), 317–30.
- Olafsdottir, H Freyja, Barry, Caswell, Saleem, Aman, Hassabis, D, & Spiers, Hugo. 2015. Hippocampal place cells construct reward related sequences through unexplored space. *elife*, **4**(01).
- Olafsdottir, H Freyja, Carpenter, Francis, & Barry, Caswell. 2016. Coordinated grid and place cell replay during rest. *Nature neuroscience*, **19**(04).
- Omer, David, Maimon, Shir, Las, Liora, & Ulanovsky, Nachum. 2018. Social place-cells in the bat hippocampus. *Science (new york, n.y.)*, **359**(01), 218–224.
- Pastoll, Hugh, Solanka, Lukas, van Rossum, Mark, & Nolan, Matthew. 2013. Feedback inhibition enables theta-nested gamma oscillations and grid firing fields. *Neuron*, **77**(01), 141–54.
- Raudies, Florian, Brandon, Mark P, Chapman, G William, & Hasselmo, Michael E. 2015. Head direction is coded more strongly than movement direction in a population of entorhinal neurons. *Brain research*, **1621**(Sept.), 355–367.
- Reifenstein, Eric, Kempster, Richard, Schreiber, Susanne, Stemmler, Martin, & Herz, Andreas. 2012. Grid cells in rat entorhinal cortex encode physical space with independent firing fields and phase precession at the single-trial level. *Proceedings of the national academy of sciences of the united states of america*, **109**(04), 6301–6.

- Sarel, Ayelet, Finkelstein, Arseny, Las, Liora, & Ulanovsky, Nachum. 2017. Vectorial representation of spatial goals in the hippocampus of bats. *Science*, **355**(01), 176–180.
- Sargolini, Francesca, Fyhn, Marianne, Hafting, Torkel, McNaughton, Bruce, Witter, Menno, Moser, May-Britt, & Moser, Edvard. 2006. Conjunctive representation of position, direction, and velocity in entorhinal cortex. *Science (new york, n.y.)*, **312**(06), 758–62.
- Sharp, Patricia. 1999. Comparison of the timing of hippocampal and subicular spatial signals: Implications for path integration. *Hippocampus*, **9**(01), 158–72.
- Stackman Jr, Robert, & Taube, Jeffrey. 1998. Firing properties of rat lateral mammillary single units: Head direction, head pitch, and angular head velocity. *The journal of neuroscience : the official journal of the society for neuroscience*, **18**(12), 9020–37.
- Stemmler, Martin, Mathis, Alexander, & Herz, Andreas. 2015. Connecting multiple spatial scales to decode the population activity of grid cells. *Science advances*, **1**(12), e1500816–e1500816.
- Stensola, Hanne, Stensola, Tor, Solstad, Trygve, Frland, Kristian, Moser, May-Britt, & Moser, Edvard. 2012. The entorhinal map is discretized. *Nature*, **492**(12), 72–78.
- Sugar, Jrgen, & Moser, May-Britt. 2019. Episodic memory: Neuronal codes for what, where, and when. *Hippocampus*, **29**(12), 1190–1205.
- Taube, Jeffrey, Muller, Robert, & Ranck, Jr, James. 1990. Head-direction cells recorded from the postsubiculum in freely moving rats. ii. effects of environmental manipulations. *The journal of neuroscience : the official journal of the society for neuroscience*, **10**(03), 436–47.
- Trettel, Sean G., Trimper, John B., Hwaun, Ernie, Fiete, Ila R., & Colgin, Laura Lee. 2019. Grid cell co-activity patterns during sleep reflect spatial overlap of grid fields during active behaviors. *Nature neuroscience*, **22**(4), 609–617.
- Wilson, M.A., & McNaughton, Bruce. 1994. Reactivation of hippocampal ensemble memories during sleep. *Science (new york, n.y.)*, **265**(08), 676–9.
- Yartsev, Michael M., Witter, Menno P., & Ulanovsky, Nachum. 2011. Grid cells without theta oscillations in the entorhinal cortex of bats. *Nature*, **479**(7371), 103–107.
- Zutshi, Ipshita, Leutgeb, Jill K, & Leutgeb, Stefan. 2017. Theta sequences of grid cell populations can provide a movement-direction signal. *Current opinion in behavioral sciences*, **17**(Oct.), 147–154.

## 6 Miscellaneous

### 6.1 Acknowledgements

I would like to thank my supervisor, Andreas Herz for all the support over the years of the PhD, whether it was scientific or personal. His guidance and motivation to explore more and improve my precision standards have contributed to turn me from a science enthusiast to a published scientific author. Additionally, I would like to highlight the role of Anton Sirota, who supported me as an additional first supervisor during my defense.

Furthermore, I would like to express my gratitude to my TAC committee, Laura Busse and Christian Leibold, whose fresh ideas and guidance for my PhD project were highly valuable.

I would also like to thank the Graduate School of Systemic Neurosciences and the Bernstein Network for providing a financial frame for my Ph.D. project. With that I would like to also thank Lena Bittl, Stefanie Bosse, Nadine Hamze, Monika Volk and Benedikt Grothe to provide guidance with the university administration.

My colleagues in the lab have given me very valuable scientific input. The postdocs, Martin Stemmler, Stefan Hausler and Kay Thurley contributed with a lot of ideas to my progress reports, to increase the statistical reliability of my projects. The students also inspired me with a lot of creative ideas as well as provided a great atmosphere to work. I would like to emphasize the influence of the conversations about science with Johannes Nagele, Michaela Poth, Avleen Sahni, Florian Eberhardt, Maximilian Winter and Chris Kymn.

Additionally, I would like to express my gratitude to Michael Myoga, András Csordás, Gábor Csordás, and András Ecker who proofread this thesis and contributed with conceptual input and corrected the grammatical mistakes.

I would like to thank all the fellow GSN students and other friends for the out-of-box ideas and the emotional support they always surrounded me with, while sailing the stormy ocean of my graduate studies. And last but not least I would like to thank my family, for inspiring me for doing a Ph.D. and then to never give up, even if it felt challenging for a moment.



## 6.2 Curriculum Vitae

# Dóra Csordás

*Data Scientist, Computational Neuroscientist*

---

## Personal Profile

Ph.D. level computational neuroscientist with competent Python programming skills. Experienced in machine learning, statistical analysis and modeling of big biological datasets.

Ran scientific projects both independently and in a team.

Eager to find creative solutions to complex problems even within tight deadlines.

Skilled at cross-hierarchical and international communication and at presentation.

Achieved excellent academic results and published in a peer-reviewed journal.

---

## Experience

### Vocational

2015–2020 **Ph.D. in Computational Neuroscience**, *Graduate School of Systemic Neurosciences, Ludwig-Maximilians-Universität München*, Munich, Defended: October, 2020.

Supervisors Prof. Dr. Andreas Herz, Prof. Dr. Anton Sirota

Description Independently pre-processed and structured biological big datasets. Applied frequently used data science methods (regression analysis, PCA, clustering, etc.) and statistical tests to the data. Presented the visualized data and the results at multiple meetings and conferences.

Publications Spike Afterpotentials Shape the In-Vivo Burst Activity of Principal Cells in Medial Entorhinal Cortex, published in *Journal of Neuroscience* (Csordás et al., 2020)  
Grid Cells Anticipate the Animal's Future Movement (Csordás et al., in prep.)

2014–2015 **Research Fellow**, *Institute of Experimental Medicine, Hungarian Academy of Sciences, Team of Dr. Szabolcs Káli, Lab. of Prof. Dr. Tamás Freund*, Budapest. Computational modeling of the network of the hippocampal formation.

### Miscellaneous

2016–2018 **Ph.D. Student Representative**, *Graduate School of Systemic Neurosciences*, Munich.

Cross-hierarchical coordination, hiring process participant, event organization, mentoring.

2012–2017 **Teaching Assistant**, *Pázmány Péter Catholic University, Ludwig-Maximilians-Universität München*, Budapest, Munich.

Basic Calculus (tutoring 20 students), Introduction to Neurobiology (tutoring 80 students), Neural Dynamics and Computation (supervision of a student)



---

## IT skills

Programming	<b>Python (advanced), Matlab, SQL, C++ (experienced).</b>
Softwares	<b>PyCharm, Mathworks Matlab, TeXstudio, NEURON.</b>
Data Analysis	<b>Statistical testing, Correlations, Linear regression, Multi-Dim. Array Operations (Numpy), Signal Processing and Statistics (Scipy), Multiprocessing.</b>
Machine Learning	<b>Deep Learning, PCA, K-means Clustering (Scikit-learn), PyTorch, Regression Analysis, Image classification, Segmentation.</b>
Visualization	<b>Matplotlib, Seaborn, Inkscape.</b>
Image Proc.	<b>Ndimage, Scikit-image.</b>
Text Editing	<b>LaTeX, Microsoft Office, Libre Office.</b>
Systems	<b>Ubuntu, Windows.</b>

---

## Education

2015–2020	<b>Fast-track Ph.D. in Neuroscience</b> , <i>Graduate School of Systemic Neurosciences, Ludwig-Maximilians-Universität München</i> , Munich.
2015 spring	<b>Erasmus Scholar student</b> , <i>Graduate School of Systemic Neurosciences, Ludwig-Maximilians-Universität München</i> , Munich.
2011–2015	<b>Molecular Bionics Engineering B.Sc.</b> , <i>Pázmány Péter Catholic University and Semmelweis University</i> , Budapest, Grade: Excellent (> 80%).

---

## Awards and Scholarships

2018	Selected poster presenter: <i>Grid cell meeting 2018 UCL</i> with Nobel laureate attendees
2015	Erasmus Scholarship to Ludwig-Maximilians-Universität München
2014	1 <sup>st</sup> prize at the Scientific Students' Associations Conference for B.Sc. thesis
2014 Mar., Oct.	Professional Science and Public Life Scholarship of Faculty at Pázmány Péter Catholic University

---

## Mentoring and Volunteering

Salsa training	Training a group of 10 trainees with a yearly stage performance for 300 people
Event organization	LMU-Harvard Young Scientists' Forum and Graduate School of Systemic Neurosciences social events, civil and green events in Munich for Hungarians
Sci. Outreach	FORSCHA 2019 Science Fair Munich, Kids Brain Day 2016 Munich

---

## Languages

English	C1, TOEFL: 98/120 (Fluent)	German	B2 (Fluent)
Hungarian	native speaker		

---

## Interests

Dancing	Training and performing Salsa, Modern jazz, Tango Argentino
Board games	Logical games like Qwirkle and Ubongo

### 6.3 List of Publications

Dóra É. Csordás, Caroline Fischer, Johannes Nagele, Martin Stemmler and Andreas V. M. Herz. Spike afterpotentials shape the *In Vivo* burst activity of principal cells in medial entorhinal cortex. *J. Neurosci.*, 40(23):4512-, June 2020

Link to the paper: <https://www.jneurosci.org/content/40/23/4512>

\*Authors do not need to obtain permission to reuse their material, including to: articles in theses or dissertations (<https://www.jneurosci.org/content/rights-permissions>).

## 6.4 Declaration of Author Contributions

Spike afterpotentials shape the *in vivo* burst activity of principal cells in medial entorhinal cortex.

In: *Journal of Neuroscience* (2020), accepted April 11, 2020. This work was designed by Dóra Éva Csordás, Caroline Fischer, Johannes Nagele, Martin Stemmler and Andreas Herz. Dóra Éva Csordás, Caroline Fischer and Johannes Nagele performed research and analyzed data (shared first authors). Andreas Herz wrote and edited the manuscript with support from Martin Stemmler and the other authors.

Grid cells anticipate the animals future movement.

This work was designed by Dóra Éva Csordás, Johannes Nagele, Martin Stemmler and Andreas Herz. Research, programming and data analyses were performed by Dóra Éva Csordás. The manuscript was written by Dóra Éva Csordás and Andreas Herz and edited by Johannes Nagele and Martin Stemmler.

---

Dóra Éva Csordás

*Author of this dissertation*

---

Prof. Dr. Andreas Herz  
or Prof. Dr. Anton Sirota  
*Supervisor*

*Munich,*